View metadata, citation and similar papers at core.ac.uk

brought to you by CORE

provided by HAL-CEA

Ghost force reduction and spectral analysis of the 1D bridging method

Guillaume Anciaux, Olivier Coulaud, Jean Roman, Gilles Zerah

To cite this version:

Guillaume Anciaux, Olivier Coulaud, Jean Roman, Gilles Zerah. Ghost force reduction and spectral analysis of the 1D bridging method. [Research Report] RR-6582, INRIA. 2008. <inria-00300603>

HAL Id: inria-00300603

https://hal.inria.fr/inria-00300603

Submitted on 18 Jul 2008

HAL is a multi-disciplinary open access archive for the deposit and dissemination of scientific research documents, whether they are published or not. The documents may come from teaching and research institutions in France or abroad, or from public or private research centers.

L'archive ouverte pluridisciplinaire **HAL**, est destinée au dépôt et à la diffusion de documents scientifiques de niveau recherche, publiés ou non, émanant des établissements d'enseignement et de recherche français ou étrangers, des laboratoires publics ou privés.

INSTITUT NATIONAL DE RECHERCHE EN INFORMATIQUE ET EN AUTOMATIQUE

Ghost force reduction and spectral analysis of the 1D bridging method

Guillaume Anciaux — Olivier Coulaud — Jean Roman — Gilles Zerah

N° 6582

Juillet 2008

Thème NUM

Rapport de recherche

ISSN 0249-6399 ISRN INRIA/RR--6582--FR+ENG

INSTITUT NATIONAL DE RECHERCHE EN INFORMATIQUE ET EN AUTOMATIQUE

INRIA

centre de recherche BORDEAUX - SUD OUEST

Ghost force reduction and spectral analysis of the 1D bridging method

Guillaume Anciaux * , Olivier Coulaud† , Jean Roman† , Gilles Zerah‡

Thème NUM — Systèmes numériques
Équipes-Projets ScAlApplix

Rapport de recherche n° 6582 — Juillet 2008 — 41 pages

Abstract: In this paper we study the Bridging Method recently developed by T. Belytschko and S. Xiao to couple continuum mechanics with molecular dynamics. This method uses an overlap zone where both models exist and where degrees of freedom are coupled. We analyze the method in the 1D case. Firstly, we show that the spatial weighting of the potential energy leads to some appreciable numerical artifacts. Then, after presenting a modification of the time integration scheme that removes such spurious effects, we introduce the method employed to numerically measure the wave reflection rates. The limitation of these reflections constitute a major issue in all existing coupling methods for dynamics simulations. After discussing some first results achieved from numerical measurements, we present a spectral analysis that attempts to explain the behavior of the coupling zone by treating it as an independent material. The predictions of this spectral analysis are finally compared to some parametric studies issued from 1D coupling simulations..

Key-words: multiscale method, atomistic-to-continuum coupling, coupling method

* Ecole Polytechnique Fédérale de Lausanne (EPFL), Faculté ENAC, Laboratoire de Simulation en Mécanique des Solides, CH-1015 Lausanne, Switzerland.
† INRIA, ScAlApplix project, 351 cours de libération, F-33405 Talence Cedex, France.
‡ CEA-DAM Ile de France, Département de Physique Théorique et Appliquée, Bruyères-le-Châtel, 91297 Arpajon Cedex.

Centre de recherche INRIA Bordeaux – Sud Ouest
Domaine Universitaire - 351, cours de la Libération 33405 Talence Cedex
Téléphone : +33 5 40 00 69 00

Réduction des forces fantomes et analyse spectral de la “bridging method” en 1D

Résumé : Dans ce rapport, nous étudions la méthode multi échelles, “bridging method”, récemment développée par T. Belytschko and S. Xiao. Cette dernière couple une échelle continue avec une échelle atomique et utilise pour cela une zone de recouvrement où les deux modèles existent et où les degrés de liberté sont couplés. Nous analysons la méthode en dimension 1. Premièrement, on montre que la pondération spatiale de l’énergie potentielle conduit à d’importants artefacts numériques. Nous introduisons alors une modification du schéma d’intégration en temps qui élimine ces artefacts. Puis, nous présentons la méthode utilisée pour mesurer numériquement les taux de réflexion d’onde ainsi que des résultats numériques justifiant nos choix. Ensuite, nous détaillons une analyse spectrale du système multi échelles qui donne un début d’explication à certains comportements du matériau hybride. Pour terminer, les résultats de l’analyse spectrale sont comparés à des simulations numériques.

Mots-clés : Méthode multi-échelle, Couplage Atomique-Continu, méthode de couplage

Contents

1 Introduction **4**

2 Ghost force analysis **8**
2.1 Ghost force reduction 8
2.2 Numerical approach 12
2.2.1 Wave propagation for an atomistic domain 14
2.2.2 Measurement of the reflection rate 16

3 Coupled governing equations **20**
3.1 Constrained velocity update 21
3.1.1 Discrete constraint values 24
3.2 Governing equations 25

4 Spectral results **30**
4.1 Spectrum modes of the coupling model 30
4.2 Dissipation of the coupling model 31
4.3 Transmission of the coupling model 33
4.4 Correlation with finite element size 33
4.5 Study of the dependence on the past history 34
4.5.1 Eigenvalues of the matrix Q 36
4.5.2 Reflection rates with respect to the history factor 36

5 Conclusion **38**

1 Introduction

Concurrent multiscale methods are a powerful tool to simulate with a low computational cost the local phenomena that occur at a scale as small as the atomic one. Such methods are commonly used to study crack propagations, dislocations, nanoindentations, contact problems [1, 19, 13, 15]. In these approaches, one couples an atomic description, which models the material at the finest scale, with a macroscopic model like continuum elasticity. The continuum elasticity equations are discretized by the finite element method with linear approximation. The macroscopic representation of the material allows considerable reduction of the number of unknowns to manipulate. Moreover, as it is easier to apply force fields on macro-models, this type of coupling can provide useful complex boundary conditions to an atomistic model.

In this work, we focus on improving the quality of the transitions between a local energy macro-model and a non local micro-model. For the local phenomena commonly represented at the finest scale, the main difficulty is to prevent the micro-model waves from being *trapped*, as the macro-model cannot represent them. Typically we obtain spurious modes such as wave reflections [9, 10]. The Quasi Continuum method [14] allows quasi-static progressions to equilibrium using a spatial zone where the forwarded information from one model to the other is reduced to a set of points called the interface zone. The concurrent coupling of length scales developed by Abraham [8] uses a seamless interface between the coupled models with a truncated energy of the degrees of freedom at this interface. The main drawback of this method is that we must refine the mesh to the micro-scale. An overview of these methods can be found in [6, 10].

Recent papers present a new approach for an atomistic to continuum (AtC) coupling with an overlap region only for the time-independent problem. Paper [5] presents an analysis of the Arlequin method for a one dimensional model problem. In [4] the authors propose a novel mathematical framework to build efficient scheme. But due to their static approach, the main problem of wave reflections is not studied.

In this paper we focus on the coupling method that was introduced by T. Belytschko and S. Xiao in [7]. It is based on a "handshake" region where the continuum and the atomistic models are both valid and are combined by using a weighting function for the energy. From now, we will refer to the overlapping region as to the bridging zone. The two models are glued together by constraining the degrees of freedom (DOFs) in order to have a coherent dynamics. To fix the notations, we consider the figure 1 with a plane coupling, where Ω^A (resp. Ω^C) is the atomic domain (resp. the finite element domain) in d-dimension and where $\Omega^R = \Omega^A \cap \Omega^C$ is the bridging zone. This overlap allows us to change the predominance of each model so that the constraint can take effect gradually when the overlap is crossed.

The method is based on a global Hamiltonian given by the sum of the two Hamiltonians referring to the two coupled domains. Moreover, to avoid to count twice the energy in the bridging zone, we introduce a weighted sum of the Hamiltonians in this region. The weighting function α is defined at each point of the bridging zone space. If we consider the $(d-1)$ dimensional manifold separating Ω^R from $\Omega^A \setminus \Omega^R$ named Γ^R, then the weighting value $\alpha(x)$ for a given point $x \in \Omega^R$ is the normalized distance $l(x)/R$ of that point to Γ^R (cf. Figure 1).

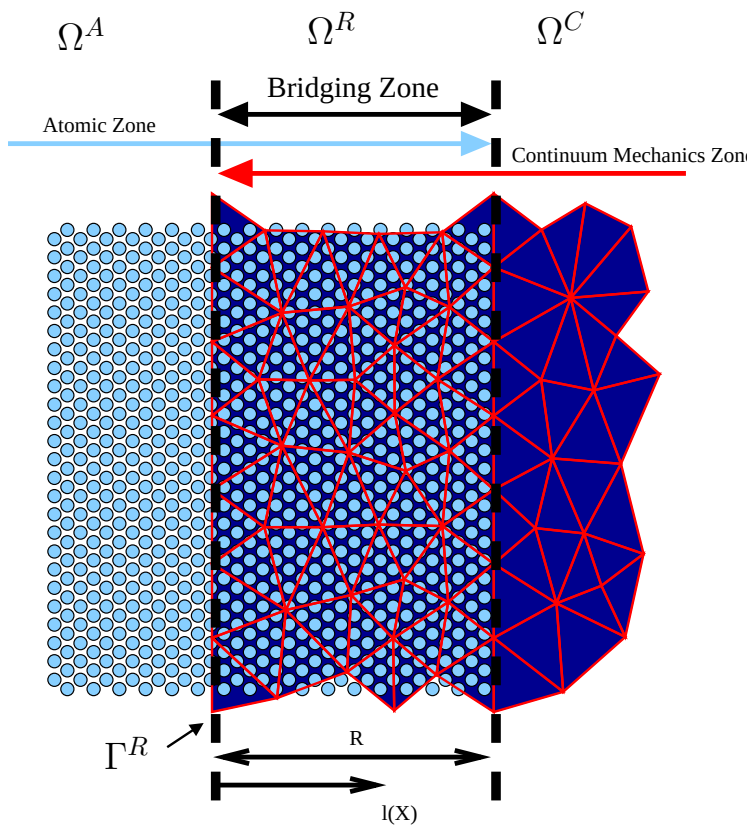

Figure 1: Plane coupling zone. Atomic domain is on the left side while continuum mechanics domain is on the right side. The bridging zone is used to define the weighting function $\alpha(X) = l(X)/R$.

Then, the global discretized multiscale Hamiltonian is

$$H_{ms} = \tilde{E^A} + \tilde{E^C},$$

where $\tilde{E^A}$ is the atomic contribution to the Hamiltonian while $\tilde{E^C}$ is the continuum contribution. More precisely, we have

$$\tilde{E^A} = \sum_{\mathbf{q}_i \in \Omega^A \setminus \Omega_R} E_i(\mathbf{q}_{\Omega^A}) + \sum_{\mathbf{q}_i \in \Omega^R} (1-\alpha(\mathbf{X}_i)) E_i(\mathbf{q}_{\Omega^R}),$$

$$\tilde{E^C} = \sum_{e \in \Omega^C \setminus \Omega_R} E_e(\mathbf{u}_{\Omega^C}) + \sum_{e \in \Omega^R} \int_e \alpha(\mathbf{X}) \delta E_e(\mathbf{u}_{\Omega^R}) \mathbf{dX},$$

where E_i is the energy fraction for atom i, $\mathbf{X}_i$ its initial position, E_e the energy fraction for element e and δE_e its potential energy density that can be computed by using the Cauchy-Born rule [18]. Here the notation $\mathbf{q}$ represents the vector of atomic positions and the notation $\mathbf{u}$ represents the nodal displacements vector. The notations $\mathbf{q}_{\Omega^A}$, $\mathbf{q}_{\Omega^R}$, $\mathbf{u}_{\Omega^C}$ and $\mathbf{u}_{\Omega^R}$ refer to spatial zones: they are used to indicate that a subset of the DOFs is considered with a geometrical point of view. Moreover, we consider indexes in upper case and in lower case to refer to finite element quantities and atomic quantities respectively.

To couple the two models, we constrain each atom into Ω^R to have the position of a virtual associated atom which is deduced from finite element interpolation. The formalism introduced by S. Xiao in [7] uses a constrained molecular dynamics algorithm to implement this. The coupling is brought by means of the following Lagrange constraint formulation: if there are L atoms in Ω^R, then we introduce the L following constraints $\mathbf{g} = \{\mathbf{g}_i\}_{i=1}^L$

$$\mathbf{g}_i = \mathbf{U}(\mathbf{X}_i) - \mathbf{d}_i = \sum_J \varphi_J(\mathbf{X}_i)\mathbf{u}_J - \mathbf{d}_i = \mathbf{0} \tag{1}$$

where $\mathbf{d}_i$ is the displacement of atom i, $\mathbf{U}(\mathbf{X}_i)$ is the macroscopic displacement evaluated by interpolation at atom i and $\mathbf{u}_J$ is the nodal displacement at node J.

We define the Lagrangian $H_L = H_{ms} + \sum_{i=1}^L \lambda_i \mathbf{g}_i$ and we denote $\Lambda = (\lambda_i)_{1,\dots,L}$ the vector of Lagrange multipliers. The governing equations are naturally modified by those multipliers as presented in [7], and provide a constrained relation between acceleration $\ddot{\mathbf{u}}_I$ (resp. $\ddot{\mathbf{d}}_i$) for continuum DOFs (resp. atomic DOFs) with forces f_I^R (resp. f_i^R) as follows

$$\begin{cases} \hat{M}_I \ddot{\mathbf{u}}_I = -\mathbf{f}_I^R + \displaystyle\sum_{k=1}^L \lambda_k \frac{\partial \mathbf{g}_k}{\partial \mathbf{u}_I}, \\ \hat{m}_i \ddot{\mathbf{d}}_i = \mathbf{f}_i^R + \displaystyle\sum_{k=1}^L \lambda_k \frac{\partial \mathbf{g}_k}{\partial \mathbf{d}_i}, \end{cases}$$

where $\hat{M}_I = \alpha(X_I) M_I$ and $\hat{m}_i = (1-\alpha(X_i)) m_i$, considering that M_I is the lumped mass on node I and m_i is the mass of atom i.

In the case of a two-body potential, the forces are given by

$$\begin{aligned} \mathbf{f}_I^R &= \sum_{e \in \mathcal{E}^I} \int_e \alpha(\mathbf{X}) \delta E_e(\mathbf{u}_e) \\ \mathbf{f}_i^R &= \sum_{\mathbf{q}_k \in \mathcal{B}_{cut}^i} \left[1 - \frac{\alpha(\mathbf{X}_i) + \alpha(\mathbf{X}_k)}{2} \right] \frac{\partial W(\mathbf{q}_i, \mathbf{q}_k)}{\partial \mathbf{q}_i} \end{aligned} \tag{2}$$

with $\mathcal{E}^I$ the set of elements containing node I, $\mathbf{u}_e$ the displacement vector of nodes owned by element e and $\mathcal{B}^i_{cut}$ the interval centered on atom i and of length $2 \cdot R_{cut}$, and R_{cut} the radius of the spherical cutoff used to evaluate the potential and the forces.

The time integration of the motion equations is done by the SHAKE algorithm [17] in which the velocities are corrected to satisfy the constraint rather than the position as in the classical algorithm. The authors claim in [7] that if the two models are consistently coupled in the initial state - which means equivalent displacement and velocity fields - and if only the velocities are coherently constrained, then the constraint on displacements will be verified during the whole simulation.

The computation of the multipliers is done by solving the linear system

$$H\Lambda = \mathbf{g}^\star$$

where H is the $L \times L$ matrix and $\mathbf{g}^\star$ is the vector of dimension L defined by

$$\begin{aligned} H_{ik} &= \Delta t \left(\sum_J \varphi_J(\mathbf{X}_I) \hat{M}_J{}^{-1} \frac{\partial \mathbf{g}_k}{\partial \mathbf{u}_J} - \hat{m}_I^{-1} \frac{\partial \mathbf{g}_k}{\partial \mathbf{d}_i} \right), \\ \mathbf{g}_i^\star &= \sum_J \varphi_J(\mathbf{X}_I) \dot{\mathbf{u}}_J^\star - \dot{\mathbf{d}}_i^\star, \end{aligned}$$

where $u^\star, d^\star$ are the displacement obtained after one time step by the integration scheme when the constraints are not applied.

For more details on this method we invite to read [7] which refers to the article presenting the original method. For example, it was suggested that a condensation process, applied to the constraint system, speeds up the calculations. The proposed condensation was a diagonal one such that

$$\tilde{H}_{ij} = \begin{cases} \displaystyle\sum_{p=1}^{L} H_{ip} & si\ i = j, \\ 0 & otherwise. \end{cases}$$

However several points that were not developed by the authors of the method can be highlighted:

- the weighting of the potential energy induces an intrusive weight on each atomic interaction. This leads to two drawbacks. The first one is the creation of spurious forces also called ghost forces [10]. The second one is that from the implementation point of view, it induces a necessary correction of all potentials. Indeed, the spatial weighting of the potential energy leads to a modification of each pair interactions. Then in order to implement the algorithm that computes the sum of forces, we have to propagate modifications to each pair potentials.
- the filtering introduced by this coupling method is not perfect and mainly depends on domain parameters like finite element sizes, time step Δt, etc...
- the condensation of the constraint matrix strongly modifies the behavior of the coupling method and especially the treatment of wave reflections.

The goal of this paper is to do a one-dimensional analysis of the original method and to propose some improvements in order to overcome several of the previous drawbacks. The paper is organized as follows. In the first part, we introduce the ghost forces in the original model that are the consequences of the spatial energy weighting and of the non locality of the atomic forces. We introduce a possible approximation which will be acceptable for large enough overlapping sizes. To fully justify this approach and introduce some preliminary results concerning wave reflections, we present numerical results from the parametric study of key values of the coupling. The second part describes the approach chosen to find the governing equations solved in the coupled region. An harmonic formulation will be exhibited and then studied in the last part ; the admitted modes of the coupling, the cutoff frequency and other considerations will be discussed before concluding this article with open perspectives.

2 Ghost force analysis

2.1 Ghost force reduction

We consider the equilibrium configuration of an argon atom chain as presented in figure 2. We can write each atomic equilibrium position as a multiple of the interatomic distance r_0 given by $X_i = ir_0$. In this configuration, the force

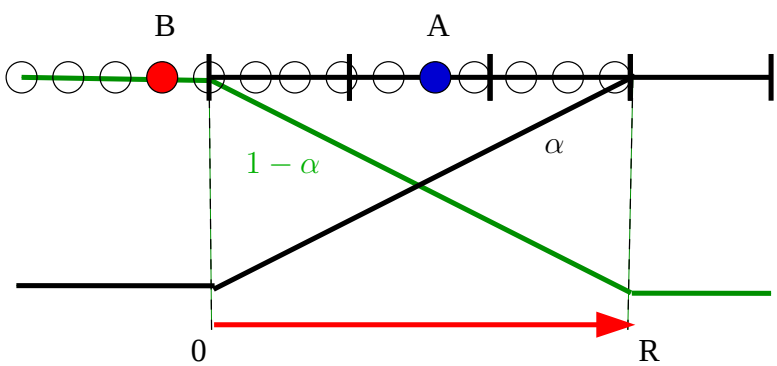

Figure 2: The coupling zone at the atomic equilibrium.

applied to atom i according to equation (2) is

$$f_i^R = \sum_{|(k-i)r_0|<R_{cut}} \left[1 - \frac{\alpha(ir_0)+\alpha(kr_0)}{2}\right] \frac{\partial W(\mid i-k \mid r_0)}{\partial(ir_0)}.$$

We introduce the following notation to describe atomic interactions

$$f_{i,j} = \frac{\partial W(\mid i-j \mid r_0)}{\partial(ir_0)}.$$

Then, if we consider that the weighting function α is $\mathcal{C}^{r+1}(]0,R])$ and by using its Taylor expansion at the order r, we have

$$\alpha(kr_0) = \alpha(ir_0) + \sum_{j=1}^{r} \frac{\alpha^{(j)}(ir_0)}{j!}\left[(k-i)r_0\right]^j + \mathcal{R}(ir_0),$$

where $\mathcal{R}(ir_0)$ is the remainder of the Taylor expansion at point ir_0.

By substituting this expression into the force definition, we can separate a local term and a non local one such that

$$\begin{aligned} f_i^R =& (1-\alpha(ir_0))f_i \\ & \underbrace{-\frac{1}{2}\sum_{|(k-i)r_0|<R_{cut}} \left[\sum_{j=1}^{d} \frac{\alpha^{(j)}(ir_0)}{j!} r_0^j (k-i)^j + \mathcal{R}(ir_0)\right] f_{i,k}}_{R_i}. \end{aligned}$$

So, we obtain

$$f_i^R = (1-\alpha(ir_0))f_i - R_i$$

where $f_i = \sum_k f_{i,k}$ is the force applied to atom i without considering the energy weighting.

At the equilibrium configuration without any coupling the force f_i applied to each atom has vanished. Thus, we will now focus on the non local term R_i. To evaluate the force, we consider the cutoff radius $R_{cut} = \mu\, r_0$; only atoms such that $|X_i - X_k| \leq R_{cut}$ are involved in the sum. Then the remainder expression is

$$\begin{aligned} R_i = & -\frac{1}{2}\sum_{\substack{k=i-\mu \\ k\neq i}}^{i+\mu} \left[\sum_{j=1}^{d} \frac{\alpha^{(j)}(i\ r_0)}{j!} r_0^j (k-i)^j\right] f_{i,k} \\ & + \mathcal{R}(ir_0) f_{i,k}. \end{aligned} \tag{3}$$

Consider now the linear weighting function $\alpha(x) = x/R$. For any atom i such that $\mathbf{X}_i \in\ ]\mu\ r_0, R-\mu r_0[$ we have

$$R_i = -\frac{r_0}{2R}\sum_{\substack{k=i-\mu \\ k\neq i}}^{i+\mu} (k-i) f_{i,k}. \tag{4}$$

Because the weighting function has a non continuous derivative around the edge of the bridging zone, we have to consider two cases. First, let us consider an atom A located at the center of the coupling zone (at a distance from the edges of the coupling zone higher than the cutoff radius) and an atom B outside of the bridging zone. If i is located like the point A on figure 2 then the slope of α is constant and is equal to $1/R$. The expression becomes

$$R_i = -\frac{r_0}{2R}\sum_{\substack{k=i-\mu \\ k\neq i}}^{i-1} (k-i) f_{i,k}.$$

But, as we are in an initial state of the atoms i (argon crystal at zero temperature and pressure), this enables us to say that the internal stress is zero in this initial state and by using the symmetry of crystalline conformation in our study case, we obtain

$$\forall i \quad \sum_{j\neq i} r_{ij} f_{i,j} = 0.$$

Using our notations and the given cutoff radius, this leads to

$$\forall i, \quad \sum_{\substack{j=i-\mu \\ j\neq i}}^{i+\mu} r_0(j-i) f_{i,j} = 0.$$

Then one can deduce that the resulting force f_i^R vanishes and that the equilibrium situation will be respected.
Here, the crucial assumption is that i is the index of an atom located in the center of the bridging zone. Such an atom is not subject to the influence of the change of slope of the weighting function.
Consider now the case of an atom close to the discontinuity of α'. We can consider for example the point B as presented on figure 2. With a linear weighting, the function has a discontinuity of its derivative. It is thus necessary to rewrite the expression of (4) by separating the right and the left derivatives of α at the point 0. Assuming that i is the index of the atom B, the modified force that acts on it can be written as the sum of two contributions:

$$\begin{aligned} f_i^R &= \sum_{k=i-\mu}^{0} f_{i,k} + \sum_{k=1}^{i+\mu} \left[1 - \frac{\alpha(i\ r_0) + \alpha(k\ r_0)}{2} \right] f_{i,k} \\ &= \sum_{k=i-\mu}^{i+\mu} f_{i,k} - \sum_{k=1}^{i+\mu} \left[\frac{\alpha(i\ r_0) + \alpha(k\ r_0)}{2} \right] f_{i,k}. \end{aligned}$$

The first part of the sum is simplified thanks to the fact that the α function is equal to 0 on the interval $]-\infty, (i+1)r_0]$. For the second term, we use a Taylor development of the weighting function centered on the point 0

$$\alpha(kr_0) = \underbrace{\alpha(0)}_{=0} + \frac{r_0(k-i-1)}{R}.$$

So we have

$$f_i^R = \sum_{k=i-\mu}^{i+\mu} f_{i,k} - \sum_{k=1}^{i+\mu} \left[\frac{r_0\ (k-i-1)}{2R} \right] f_{i,k}.$$

We finally obtain a simplified expression with the distinction of the *uncoupled forces* from the non local term:

$$f_i^R = f_i \underbrace{- \frac{r_0}{2R} \sum_{k=1}^{i+\mu} (k-i-1) f_{i,k}}_{R_i}.$$

When $i \geq 1-\mu$ the atom B undergoes a non null ghost force. Moreover this force *cannot* be compensated by the Lagrange constraints since this particular atom is not inside of the bridging zone. This effect influences all the atoms at a distance from the edge of the bridging zone lower than the selected cutoff radius. Thus, it induces a modified equilibrium as the figure 3 presents for the case of an atomic zone coupled with two continuum mechanics zones. This effect is directly related to the *nonlocal* behavior of the atomic interactions concurrently with the use of a local energy weighting.

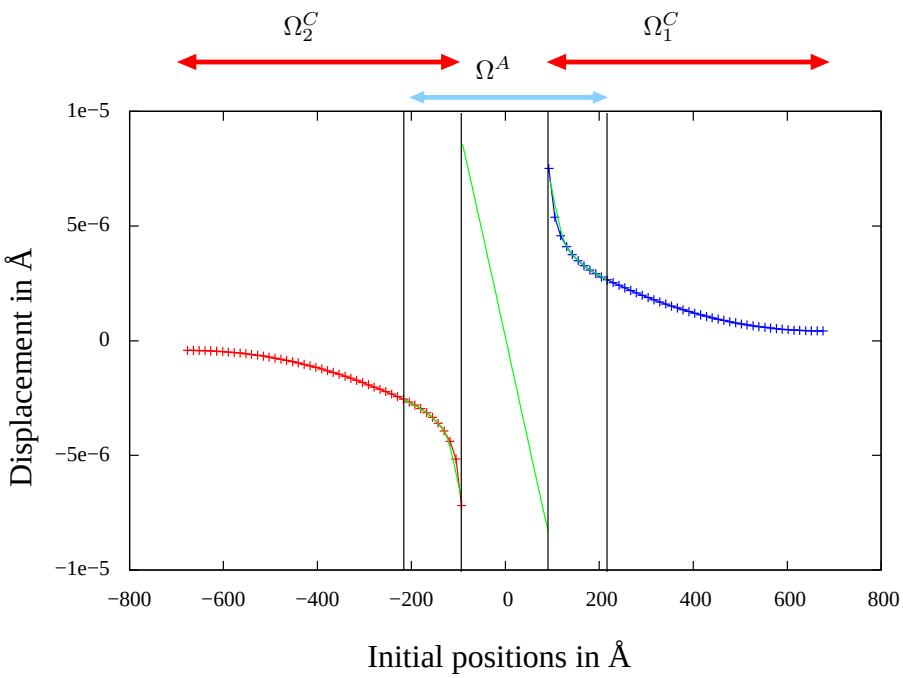

Figure 3: This figure presents the equilibrium situation obtained with a Lennard-Jones potential with a cutoff radius of $2r_0$. It is clear that the bridging zone size is too small as residual forces are induced near the edges of the coupling zone.

To improve the method, we modify the integration scheme in order to compute a suitable dynamics of the DOFs. Indeed, we did a main approximation which consisted *in neglecting the remaining force* R_i. We thus have a new expression for the governing equations of the coupled system

$$\begin{cases} \hat{M}_I \ddot{\mathbf{u}}_I = -\alpha(\mathbf{X}_I)\mathbf{f}_I + \displaystyle\sum_{k=1}^{L} \lambda_k \frac{\partial \mathbf{g}_k}{\partial \mathbf{u}_I} \\ \hat{m}_i \ddot{\mathbf{d}}_i = \alpha(\mathbf{X}_i)\mathbf{f}_i + \displaystyle\sum_{k=1}^{L} \lambda_k \frac{\partial \mathbf{g}_k}{\partial \mathbf{d}_i}, \end{cases} \tag{5}$$

where $\mathbf{g}$ is the constraint vector defined by (1). This choice is induced by the remarks stated in this section, but also by practical reasons. Indeed in molecular dynamics codes, there is no easy way to compute the weighting force contribution between two atoms which is needed in the expression (2). An other point of view for this approximation comes from the following alternative expression of system (5)

$$\begin{cases} M_I \ddot{\mathbf{u}}_I = -\mathbf{f}_I + \dfrac{1}{\alpha(X_I)} \displaystyle\sum_{k=1}^{L} \lambda_k \frac{\partial \mathbf{g}_k}{\partial \mathbf{u}_I} \\ m_i \ddot{\mathbf{d}}_i = \mathbf{f}_i + \dfrac{1}{\alpha(X_i)} \displaystyle\sum_{k=1}^{L} \lambda_k \frac{\partial \mathbf{g}_k}{\partial \mathbf{d}_i}. \end{cases}$$

This is a classical Newton governing equation and the masses are unchanged as well as the forces. The weighting impacts on the Lagrange constraints, i.e. on the coupling. What must be understood here is that only the DOFs corrections will be modified by taking into account the weighting function α and not anymore the force computation.

An additional justification to use this approximation is the following expression of the upper bound of the remainder which quantifies the error that we commit on the force computations:

$$\begin{aligned} \mid R_i \mid = \mid \frac{r_0}{2R} \sum_{k=1}^{\mu-1} k f_{i,k} \mid \leq \frac{\mu(\mu-1)r_0}{4R} \max_k \mid f_{i,k} \mid \\ \leq \frac{R_{cut}}{R} \frac{(\mu-1)}{4} \max_k \mid f_{i,k} \mid . \end{aligned}$$

In the finite element case the error made on the force calculation is

$$R_I = \sum_{e \in \mathcal{E}^I} \left(\int_e \alpha(X) \delta E_e(u_e) - \alpha_I \int_e \delta E_e(u_e) \right).$$

And with the same type of approximation that considers the weighting function as linear, we have $\alpha(X) - \alpha_I = \dfrac{X - X_I}{R}$ and we can write

$$\begin{aligned} \mid R_I \mid = \mid \sum_{e \in \mathcal{E}^I} \int_e \frac{\alpha(X) - \alpha_I}{R} \delta E_e(u_e) \mid \\ \leq \frac{h}{R} \mid \sum_{e \in \mathcal{E}^I} \int_e \delta E_e(u_e) \mid \leq \frac{h}{R} \mid f_I \mid, \end{aligned}$$

where h is the characteristic finite element size. This shows that for reasonable size of the bridging zone size R with respect to the cutoff radius and the finite element size, the residual force is small enough and thus our approximation will be valid.

2.2 Numerical approach

The main problem of the bridging method is the induced distortion of the waves propagating into the simulated material. The assumption which considers that all waves propagate similarly through the coupling zone is obviously naive. First, due to the well known dispersion equation [11, 12], we must consider that harmonic waves propagate at different speeds depending on the frequency. Secondly, the material behavior due to energy weighting and the Lagrange constraints, is more complex and can scatter waves. These phenomena will lead to wave reflections.

In order to quantify the effects of this coupling method, we first simulate the propagation of pseudo harmonic waves with a given frequency. We will then be able to produce wave propagation tests with respect to the frequency and other model parameters. Our analysis uses the kinetic energy measured and more precisely the amount of kinetic energy that is retained in the molecular dynamics zone by the coupling. To analyze our results, we compare the multiscale approach with full molecular dynamics simulations. The detailed procedure used

to build the harmonics, the measurement of wave reflection rates and the results achieved are presented in the following.
In order to carry out frequency tests, we defined disturbances which will be used as initial conditions and which have a controlled Fourier spectrum. The following displacement wave is considered

$$u_k(X,t) = \sin(kX - \omega_k\ t)\ e^{-\frac{(kX-\omega_k t)^2}{L^2}}. \tag{6}$$

where k is the characteristic wavenumber and ω_k is the angular velocity associated with k through the dispersion equation. It can be shown (see [3]) that this function is solution of a wave equation and that its spectrum is

$$\mathcal{F}_k(\xi) = \frac{\sqrt{\pi}L}{2ik}\left[e^{\frac{-(k-\xi)^2L^2}{4k^2}} - e^{\frac{-(k+\xi)^2L^2}{4k^2}}\right].$$

Figure 4 illustrates the displacement $u_1(X,0)$ and its spectrum for different

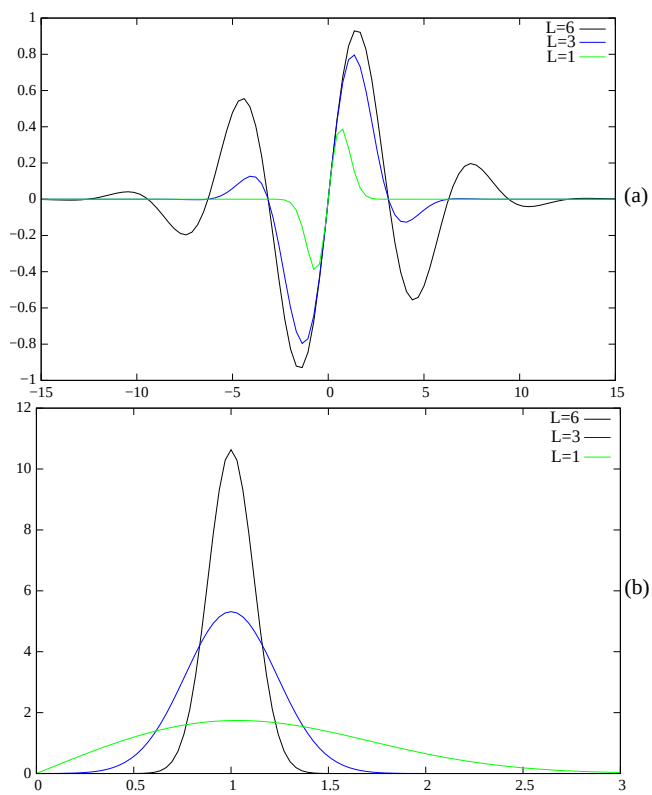

Figure 4: Figure (a) presents the form of the impulses we want to use as initial condition for our frequency test case and figure (b) its associated spectrum.

values of the parameter L which controls precisely the size of the Fourier spectrum. Choosing a too large value of L increases the spatial zone necessary to represent the wave train. The parameter L controls the bandwidth around the desired frequency and the displacement of the spectrum peak. For example, for $L = 1$, one obtains a peak centered at $1.5k$ while for $L = 3$, the shift is lower than 10^{-4}. We choose $L = 3$ for all our tests.

2.2.1 Wave propagation for an atomistic domain

Let us consider the monoatomic chain composed of 1128 argon atoms as shown in figure 5 with periodic boundary conditions and the Lennard Jones potential [2] with the following parameters: $r_0 = 1.2316$ Å; $\sigma = 1.1$ Å; $\epsilon = 1.657\ 10^{-21}$ Joules; $m = 39.95\ 10^{-3}$ Kg/mol; $R_{cut} = 2.2r_0$. The length of the domain is large enough to ensure that the initial wave centered in the domain will not interact with the image waves due to periodic boundary conditions before 20000 time steps.

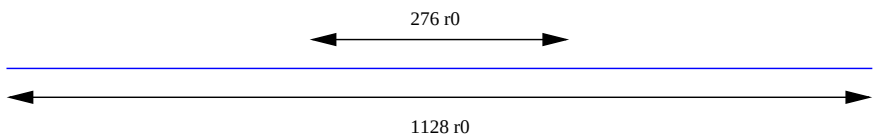

Figure 5: Atomic chain domain. We measure kinetic energy in the central area constituted by 276 atoms.

At time $t = 0$, we input the initial displacement given by (6). Two waves are then created, each one with an opposite direction and each with half the initial magnitude. This can be observed on figure 6. The kinetic energy transported can be deduced from the magnitude of the initial perturbation.

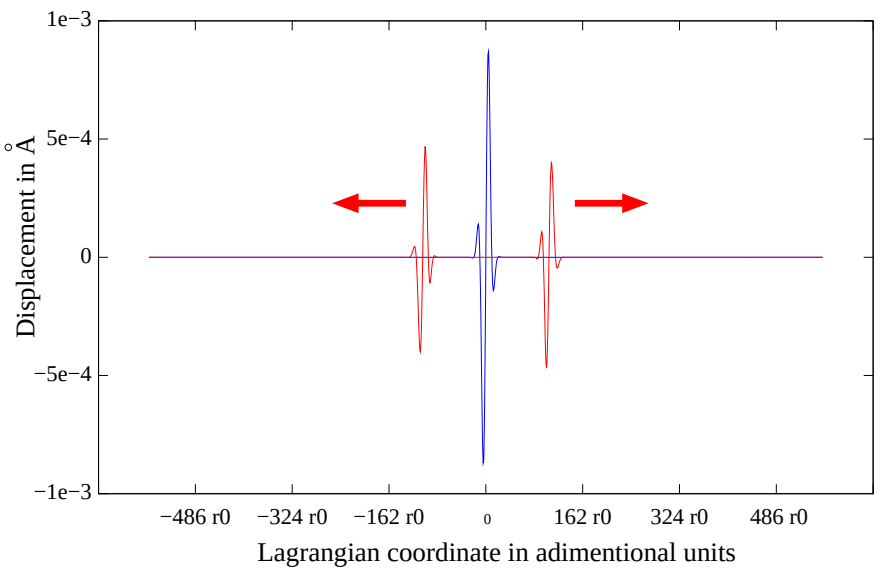

Figure 6: The wave creation process. The initial displacement, given by equation (6) with $k = 20r_0$, is plotted in blue while the displacement after 5000 time steps (10^4 femtoseconds) is plotted in red. At this time, two displacement waves are observed.

In order to quantify the wave reflections, the kinetic energy that remains confined into a given spatial zone must be measured. However, due to the dispersion in discrete materials, high frequency waves (close to the Brillouin zone) are very unstable and induce stationary waves. As a consequence, the

measured values of the kinetic energy will also contain the contribution of such stationary waves.

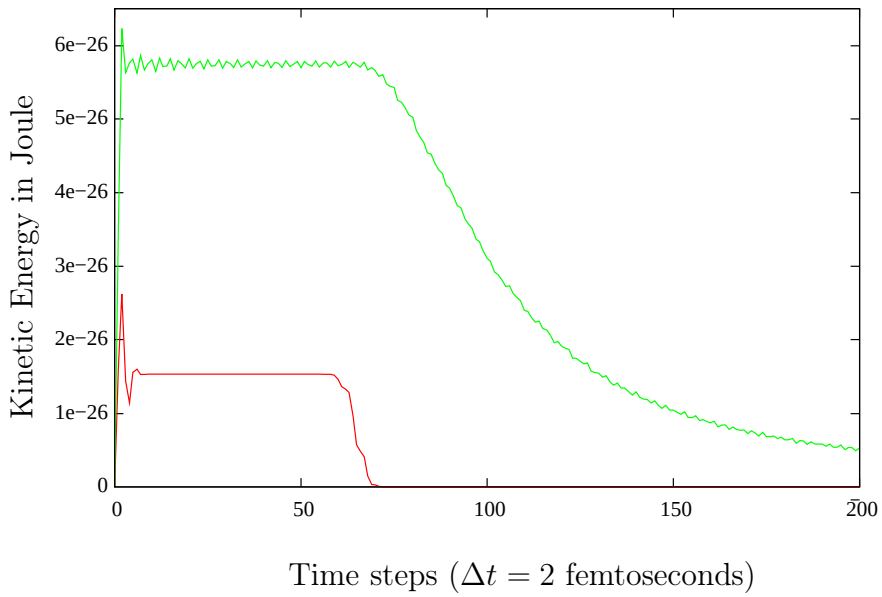

Figure 7: The kinetic energy in the region constituted by the 276 atoms in the center of the domain (see fig. 5) with respect to simulation time steps. The green curve is measured when initial harmonic is parametrized with $k = 2r_0$ while the red one is for $k = 20r_0$.

Figure 7 shows the kinetic energy of the atoms contained in the interval $[-138r_0, 138r_0]$. These atoms will be denoted as the "test" zone. We present the resulting kinetic energy for two distinct injected frequencies: the first one is for $k = 2r_0$, and the second one is for $k = 20r_0$. It can clearly be observed that there is almost no remaining kinetic energy in the test zone when using a low frequency wave ($k = 20r_0$), while for $k = 2r_0$ we measured residual amount of 10^{-26} Joules in the test zone. This is due to the dispersion of waves in the atomic chain which creates stationary waves. In other words, the initial wave scatters much more in the case of high frequencies which naturally creates some remaining kinetic energy in the center of domain.
In order to have a good idea of the energy levels involved in the process, we consider the energy created by the initial displacement that is imposed. This energy can be computed as the kinetic energy of two harmonic train waves. The kinetic energy of a set of atoms is

$$E^c = \frac{1}{2}\sum_i m_i v_i^2, \tag{7}$$

where m_i is the mass and v_i the velocity of atom i. We consider the displacement

$$u(X_i, t) = u_i = A\ sin(kX_i - \omega_k t)e^{-\frac{(kX_i - \omega_k t)^2}{L^2}},$$

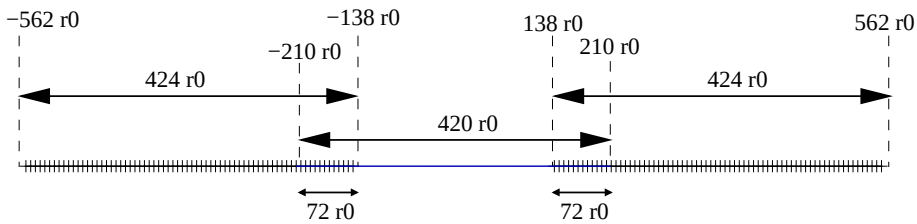

Figure 8: The molecular dynamics domain is in the center. It is coupled with two models of mechanics of the continuous mediums which are used as boundary condition.

as an initial condition. The velocities induced by an harmonic wave of half magnitude are

$$v(X_i,t) = \frac{A\omega_k}{2}\ e^{-\frac{(kX_i-\omega_k t)^2}{L^2}} \left[-\cos(kX_i-\omega_k t) + \frac{2}{L^2} sin(kX_i-\omega_k t)(kX_i-\omega_k t) \right].$$

If we consider the velocities of such a wave at initial time ($t=0$) then we have

$$v_i = \frac{A\omega_k}{2}\ e^{-\frac{(kX_i)^2}{L^2}} \left[-\cos(kX_i) + \frac{2}{L^2} sin(kX_i)(kX_i) \right].$$

And finally we can evaluate by (7) the kinetic energy transported by this wave.

We compare the values obtained with the kinetic energy measured in a full molecular dynamics simulation[1]. Once the transfer from potential energy to kinetic energy has taken place, the kinetic energy remains constant until some effect (boundary conditions for instance) induces an inverse transfer from kinetic energy to potential energy. It must be reminded that the total energy is constant. In our simulation, the "predicted" values and the kinetic energy measured after 20000 time steps are matched up to 99%. But for high frequencies ($k = 2r_0$), the instability of the wave (due to the dispersion equation) and the transfers between potential and kinetic energy lead to a real divergence between predicted and measured values. Thus in practice we use only the measured values even for $k = 2r_0$.

2.2.2 Measurement of the reflection rate

Our reference test case for a coupled simulation, initially presented in reference [7], considers a bridging size of $72r_0$, a "test" zone of $[-138r_0, 138r_0]$, and a molecular dynamics domain $[-210r_0, 210r_0]$. The continuum mechanics domain is constituted by two separated meshes for the spaces $[-562r_0, -138r_0]$ and $[138r_0, 562r_0]$. The finite element size h is constant and equal to $8r_0$. Both meshes contain 53 elements. The coupled model is depicted on figure 8.

By performing a simulation with an induced displacement wave, we can measure the kinetic energies at different stages of the simulation. On figure 9 we present the kinetic energy in the case of an important wave reflection. The scenario of the simulation has 5 stages:

[1] only with an atomistic description i.e. without any multiscale coupling

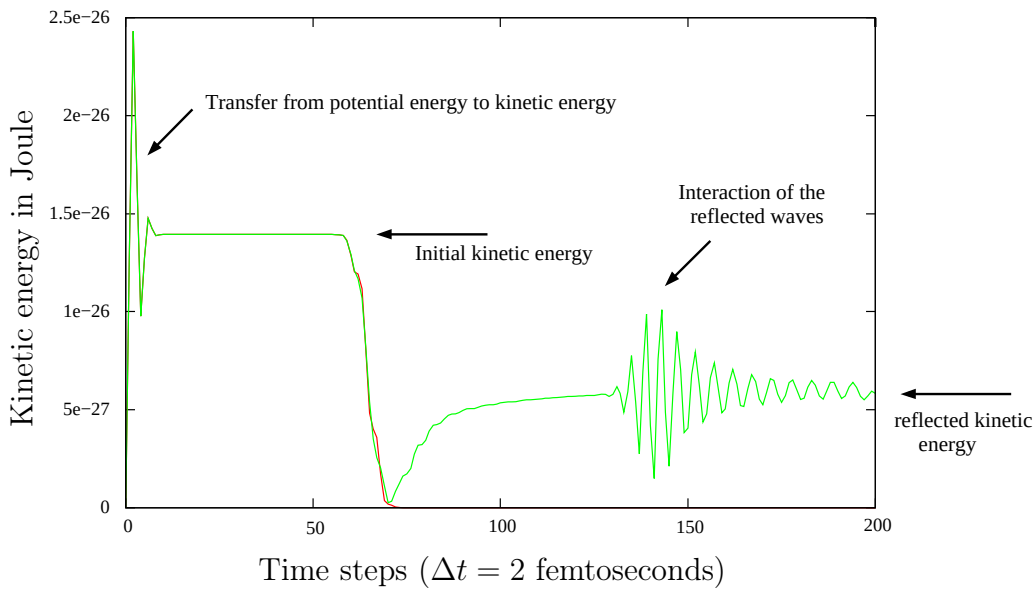

Figure 9: Measurement of the kinetic energy in the test zone with respect to time steps.

1. the initial displacement induces the creation of two waves with opposite directions with a transfer from potential energy to kinetic energy until both quantities, as well as the waves, are stable;
2. the waves propagate in the atomic domain;
3. the waves move into the coupling zone. This leads to a decrease of the level of the kinetic energy;
4. two reflected waves are created with a given amount of kinetic energy before stabilization;
5. both reflected waves interact in the center of the molecular dynamics domain creating fluctuations of the kinetic energy. These fluctuations take place around a mean value.

Now, let us define the following reflection rate:

$$R_r = \frac{K^C - K^{MD}}{K_{init}}$$

where K^{MD} is the full molecular dynamics kinetic energy measured in the test zone, K^C is the multiscale kinetic energy measured in the test zone, and K_{init} is the kinetic energy in the test zone after the creation of the initial waves (stage 2).
In the following, we present the results obtained using different values of various parameters. The potential used is Lennard-Jones with parameters: $r_0 = 1.2316$ Å; $\sigma = 1.1$ Å; $\epsilon = 1.657\ 10^{-21}$ Joules; $m = 39.95\ 10^{-3}$ Kg/mol and with

$Rcut = 2.2r_0$. All the tests presented involve a variation of the injected frequency via the wavelength parameter λ, according to the formula $k = 2\pi\lambda$. We consider the range $\lambda \in [2r_0, 60r_0]$. Furthermore, we will also present the results obtained by using our scheme which avoids ghost forces and simplifies the computation of the forces. As well as these points, we will discuss various aspects of the method influenced by parameters such as the size of the bridging zone.

Reflection rate with respect to the condensation of the constraint matrix As mentioned in [7], it is suggested to condense the constraint matrix in order to speed up the computations. The effect of such a manipulation is critical and should not be neglected. Figure 10 presents the reflection rates obtained for the coupled model. The curves labelled "Arlequin" and "New"

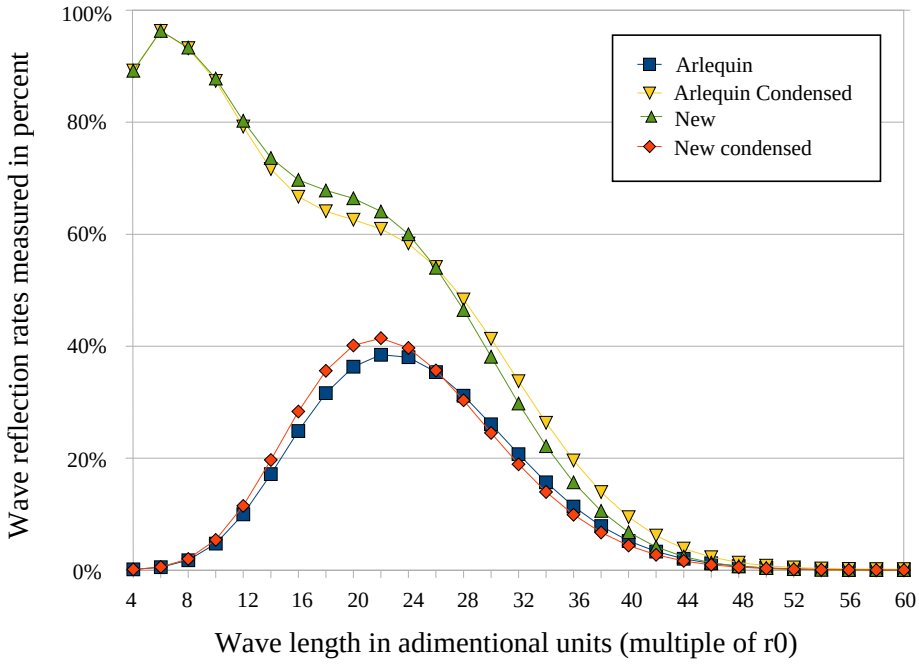

Figure 10: Reflection rates in percent of the initial wave energy with respect to harmonic wave length. These were measured on coupled numerical simulations for the Arlequin method and our formulation. Full and condensed constraint matrix cases are also presented.

refer to the reflection rates measured for the initial formulation and for the approximation we introduced (see eq. 5). Results issued from the use of the full and lumped versions of the constraint matrix are also presented.

Note the considerable enhancement achieved by the condensation of the constraint matrix in the high frequencies domain. We remind that the finite element model cannot represent the high frequencies due to the reduced number of degrees of freedom. As a consequence, strongly constraining the atoms to follow the mesh behavior naturally leads to reflection effects. However, this argument is not completely convincing from a mathematical point of view. But the spec-

tral analysis of the next section will justify more precisely this idea and will lead to a better understanding of the coupling.

Reflection rate with respect to the bridging size The size of the bridging zone controls the magnitude of wave reflections. More precisely, increasing the coupling length decreases the reflection rates. We made vary the bridging size to obtain the results presented on figures 11 and 12, considering here that the constraint system has been condensed. Figure 11 presents the reflection rates obtained, first with the initial method with intrusive forces. It can be seen that there is an upper bound of the wave reflection (43%) for the wave length $22r_0$. As expected, the rates are decreasing while the bridging size increase, but bridging sizes $32r_0$, $64r_0$ and $72r_0$ give similar results.

Figure 12 presents the same test set but with non intrusive force calculation. This time, the upper bound reaches 50%. With regard to the previous results, the rates are decreasing when the bridging size increases, even for low bridging sizes. For coupling lengths higher than $104r_0$, the non intrusive method gives better results than the original one. This justifies the use of the approximation leading to governing equation (5).

Due to the approximation made on the force calculation (see 2), we see spurious wave reflections for small coupling sizes. But we have clearly shown that such an approximation is valid in terms of wave reflections once the bridging size has reached a certain level.

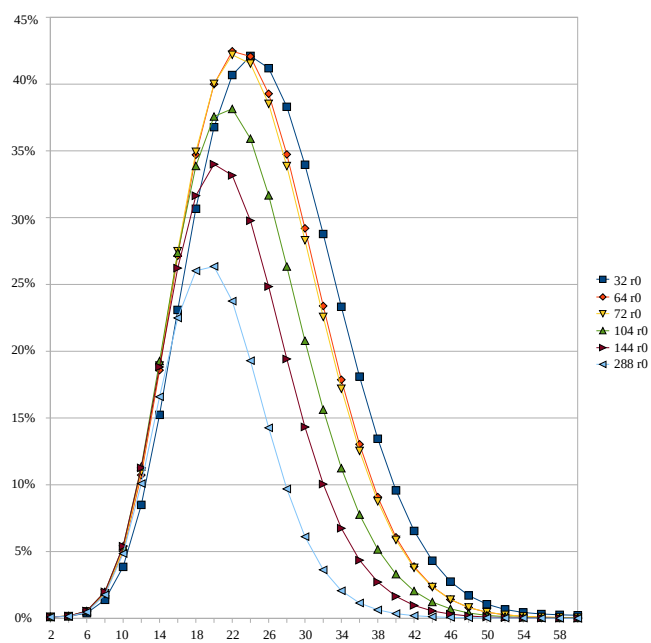

Figure 11: Reflection rates, for the bridging method, in percent of the initial wave energy with respect to the injected harmonic wave length. The different curves present the reflection rates for different overlap sizes.

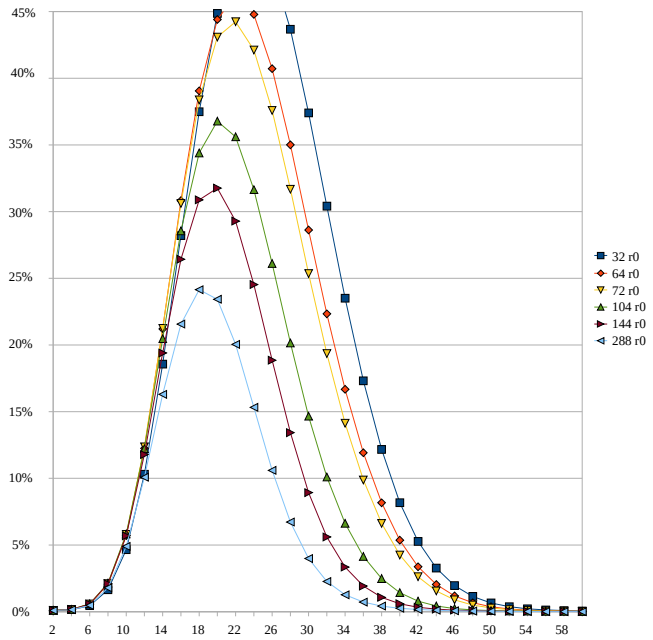

Figure 12: Reflection rates, for the bridging method with our approximation - see equation (5) - in percent of the initial wave energy with respect to the injected harmonic wave length. The different curves present the reflection rates for different overlap sizes.

3 Coupled governing equations

The coupling zone is a hybrid zone where the waves are propagated and dispersed in a specific way. The purpose of this section is to find the governing equations that are solved by our coupling approach in order to understand the effects of the coupling on wave propagation. We will then be able to explain how the wave reflections occur in the bridging zone.

In order to reach this goal, we will use a reversed approach compared to what is usually done. To find the equations governing the behavior of the coupling region, we will start from the integration scheme. Then the force linearization will allow us to study the coupling system as an harmonic oscillator.
Equations (5) are integrated by the SHAKE scheme [17], which can be written

in the following matrix form

$$\begin{cases} \dot{d}^{n+1/2} = \dot{d}^n + \dfrac{\Delta t}{2}\, m^{-1} \cdot f^n \\ \dot{u}^{n+1/2} = \dot{u}^n + \dfrac{\Delta t}{2}\, M^{-1} \cdot F^n \\ d^{n+1} = d^n + \Delta t\ \dot{d}^{n+1/2} \\ u^{n+1} = u^n + \Delta t\ \dot{u}^{n+1/2} \\ \text{evaluation of } f^{n+1} \text{ and } F^{n+1} \\ \dot{d}^{n+1} = \dot{d}^{n+1/2} + \dfrac{\Delta t}{2}\, m^{-1} \cdot f^{n+1} + \dfrac{\Delta t}{2}(\theta \cdot m)^{-1} \cdot \lambda \\ \dot{u}^{n+1} = \dot{u}^{n+1/2} + \dfrac{\Delta t}{2}\, M^{-1} \cdot F^{n+1} - \dfrac{\Delta t}{2}(\beta \cdot M)^{-1} \cdot A^t \cdot \lambda \\ \text{with } \lambda \text{ such that } \mathbf{g}(\dot{d}^{n+1}, \dot{u}^{n+1}) = 0, \end{cases} \tag{8}$$

where m and M are the diagonal mass matrices, $\mathbf{g}$ the constraint function defined in (1), A the interpolation matrix on the atomic sites and θ, β the matrices expressing the weighting functions for each model. These matrices are given by

$$A_{iJ} = \varphi_J(X_i),\ \beta_{IJ} = \delta_{IJ}\ \alpha(X_I) \text{ and } \theta_{ij} = \delta_{ij}\ (1 - \alpha(X_i)).$$

To guarantee the validity of the previous equations, we have the following strong assumption

Hypothesis: The diagonal matrices θ and β are regular.

$$\forall I = 1, N \quad \beta_{II} \neq 0 \qquad \forall i = 1, n \quad \theta_{ii} \neq 0$$

Remark: *this assumption is not valid on the boundary of the finite element domain. In fact, the weighting functions should be defined so that neither atom nor finite element node has a zero weight. In [7], the weights associated to the first element in the coupling are arbitrarily selected as non zero, and recommended to be fixed at* 10^{-3}*. Such a choice is non-trivial and has an impact on the behavior of the wave reflections. This will be discussed in section 4.5.*

3.1 Constrained velocity update

To study the computed trajectories, we consider the solution obtained by the discrete scheme (8) with a given time step Δt. We denote these trajectories by $u_{\Delta t}(t)$ and $d_{\Delta t}(t)$ for a given time t. We also suppose that these solutions converge to $u(t)$ and $d(t)$ when Δt tends towards 0. To clarify the following calculations, from now on we denote the forces by $f(d_{\Delta t}(t))$ and $F(u_{\Delta t}(t))$ to make explicit the dependence on displacements. To evaluate the velocity increment, we rewrite system (8) with an explicit time dependency

$$\begin{cases} \dot{d}(t + \Delta t) = \dot{d}(t) + \Delta t m^{-1} \hat{f}_{\Delta t} + \dfrac{\Delta t}{2} m^{-1} \theta^{-1} \cdot \lambda \\ \dot{u}(t + \Delta t) = \dot{u}(t) + \Delta t M^{-1} \hat{F}_{\Delta t} - \dfrac{\Delta t}{2} M^{-1} \beta^{-1} \cdot A^t \cdot \lambda, \end{cases} \tag{9}$$

with

$$\hat{f}_{\Delta t}(t) = \frac{f(d_{\Delta t}(t)) + f(d_{\Delta t}(t + \Delta t))}{2}$$

and

$$\hat{F}_{\Delta t}(t) = \frac{F(u_{\Delta t}(t) + F(u_{\Delta t}(t+\Delta t))}{2},$$

and λ chosen such that the constraint

$$\mathbf{g}(\dot{u}_{\Delta t}(t+\Delta t), \dot{d}_{\Delta t}(t+\Delta t)) = 0$$

is satisfied. This can be written as

$$A\ \dot{u}_{\Delta t}(t+\Delta t) - \dot{d}_{\Delta t}(t+\Delta t) = 0.$$

Using the expression of $\dot{u}_{\Delta t}$ and $\dot{d}_{\Delta t}$ one obtains

$$A\left(\dot{u}_{\Delta t}(t) + \Delta t M^{-1}\hat{F}_{\Delta t}(t) - \frac{\Delta}{2} t M^{-1}\beta^{-1}A^t\lambda\right) - \dot{d}_{\Delta t}(t)$$
$$-\frac{\Delta t}{2} m^{-1}\hat{f}_{\Delta t} - \frac{\Delta t}{2} m^{-1}\theta^{-1}\cdot\lambda = 0.$$

Then the Lagrange multipliers satisfy the system

$$\frac{\Delta t}{2}(AM^{-1}\beta^{-1}\cdot A^t + m^{-1}\theta^{-1})\cdot\lambda =$$
$$A\left(\dot{u}_{\Delta t}(t) + \Delta t M^{-1}\hat{F}_{\Delta t}\right) - \dot{d}_{\Delta t}(t) - \Delta t m^{-1}\hat{f}_{\Delta t}.$$

Let us now consider the constraint matrix H defined by

$$H = AM^{-1}\beta^{-1}\cdot A^t + m^{-1}\theta^{-1},$$

the Lagrange multipliers are the solutions of the following linear system

$$H\cdot\lambda = \frac{2}{\Delta t}\dot{g}_{\Delta t}(t) + AM^{-1}\hat{F}_{\Delta t} - m^{-1}\hat{f}_{\Delta t}$$

where $\dot{g}_{\Delta t}(t) = A\ \dot{u}_{\Delta t}(t) - \dot{d}_{\Delta t}(t)$.

Lemma 3.1 *If we assume that there are no null weight associated to any coupled degree of freedom, then H is regular.*

Proof:

The constraint matrix has the following expression:

$$H = AM^{-1}\beta^{-1}\cdot A^t + m^{-1}\theta^{-1}.$$

Let D_1 and D_2 be the diagonal matrices

$$D_1 = M^{-1}\beta^{-1} \qquad \textit{and} \qquad D_2 = m^{-1}\theta^{-1}.$$

Then we can write

$$H = AD_1A^t + D_2.$$

As the weights used are non zero by hypothesis, we have:

$$\exists\epsilon_1 > 0 \text{ and } \exists\epsilon_2 > 0 \text{ such that } \forall i \quad (D_1)_i \geq \epsilon_1 \quad \textit{and} \quad (D_2)_i \geq \epsilon_2.$$

Then, using the properties of the scalar product in $\mathcal{R}^n$, we obtain for an arbitrary chosen vector u:

$$< (AD_1A^t + D_2)u, u >=< AD_1A^tu, u > + < D_2u, u >$$

which leads to the following lower bound:

$$< (AD_1A^t + D_2)u, u > \quad \geq \quad \epsilon_1 \mid\mid A^tu \mid\mid^2 + \epsilon_2 \mid\mid u \mid\mid^2 \geq 0.$$

If H were not regular, then a vector $u \neq 0$, such that $< Hu, u >= 0$ would exist. Then:

$$\epsilon_1 \mid\mid A^tu \mid\mid^2 + \epsilon_2 \mid\mid u \mid\mid^2 = 0 \Rightarrow u = 0$$

which is a contradiction. So H is regular. ■

Now that H is proved as regular, the Lagrange multipliers are given by

$$\lambda = H^{-1}\mathcal{F}_{\Delta t}(t) + \frac{2}{\Delta t}H^{-1}\dot{g}_{\Delta t}(t) \tag{10}$$

where $\mathcal{F}_{\Delta t}(t) = AM^{-1}\hat{F}_{\Delta t}(t) - m^{-1}\hat{f}_{\Delta t}(t)$.
In order to prevent any confusion, we remind here that $\mathcal{F}_{\Delta t}(t)$ depends on the forces, hence on the position trajectories ($u_{\Delta t}$ and $d_{\Delta t}$), while $\dot{g}_{\Delta t}(t)$ depends on the velocity trajectories ($\dot{u}_{\Delta t}$ and $\dot{d}_{\Delta t}$).

As we already mentioned in the introduction, the original method [7] recommends the use of a modified version of the constraints matrix in order to speed up calculations of the Lagrange multipliers. In particular, they consider the positive definite matrix $\tilde{H}$

$$\tilde{H}_{ij} = \begin{cases} \sum_{p=1}^{L} H_{ip} & \text{if } i = j, \\ 0 & \text{otherwise.} \end{cases}$$

But this simple operation has critical consequences as we will show in the following study. Indeed, when we condense the constraint matrix H on its diagonal, we introduce implicitly an additional force which will be beneficial (c.f. section 2.2.2) to the wave reflection problem.

For sake of generality we use in the following calculations a generic matrix $\tilde{H}$ to compute the Lagrange multipliers. Let us consider again equation (10). As matrix H is approximated by $\tilde{H}$, the constraints are not guaranteed anymore to be verified at each time step. This will introduce additional forces onto the DOFs of the system. The expression of the Lagrange multipliers are now

$$\lambda = \tilde{H}^{-1}\mathcal{F}_{\Delta t}(t) + \frac{2}{\Delta t}\tilde{H}^{-1}\dot{g}_{\Delta t}(t).$$

In order to find the system verified by $(u(t), d(t))$, we write the velocity variation as follows:

$$\begin{cases} m\dfrac{\dot{d}_{\Delta t}(t+\Delta t) - \dot{d}_{\Delta t}(t)}{\Delta t} & = \hat{f}_{\Delta t}(t) + \theta^{-1}\tilde{H}^{-1}\mathcal{F}_{\Delta t}(t) \\ & +\theta^{-1}\tilde{H}^{-1}\dfrac{\dot{g}_{\Delta t}(t)}{\Delta t} \\ M\dfrac{\dot{u}(t+\Delta t) - \dot{u}(t)}{\Delta t} & = \hat{F}_{\Delta t}(t) - \beta^{-1}A^t\tilde{H}^{-1}\mathcal{F}_{\Delta t}(t) \\ & -\beta^{-1}A^t\tilde{H}^{-1}\dfrac{\dot{g}_{\Delta t}(t)}{\Delta t} \end{cases}$$

3.1.1 Discrete constraint values

According to the previous expression of the trajectories, we compute the value of the constraints in order to know the behavior imposed to the DOFs.

Lemma 3.2 *$\forall (t, \Delta t) \in \mathbb{R}_+^2$ and $\forall n \in \mathbb{N}^*$*

$$\dot{g}_{\Delta t}(t + n\Delta t)) = \frac{\Delta t}{2} \sum_{i=1}^{n} Q^i \mathcal{F}_{\Delta t}(t + \Delta t(n-i)) + Q^n \dot{g}_{\Delta t}(t).$$

Proof of the lemma. We consider the expression of the velocity constraint:

$$\begin{aligned} g(\dot{u}_{\Delta t}(t+\Delta t), \dot{d}_{\Delta t}(t+\Delta t)) =& A\dot{u}_{\Delta t}(t+\Delta t) - \dot{d}_{\Delta t}(t+\Delta t) \\ =& A\dot{u}_{\Delta t}(t) - \dot{d}_{\Delta t}(t) + \Delta t \mathcal{F}_{\Delta t}(t) \\ & - \frac{\Delta t}{2}\left[AM^{-1}\beta^{-1}A^t + m^{-1}\theta^{-1}\right]\lambda \\ =& \dot{g}_{\Delta t}(t) + \frac{\Delta t}{2}\mathcal{F}_{\Delta t}(t) - \frac{\Delta t}{2} H\lambda. \end{aligned}$$

By using the expression of the Lagrange multipliers (10), we have

$$\begin{aligned} g_{\Delta t}(t+\Delta t) =& g_{\Delta t}(t) + \Delta t \mathcal{F}_{\Delta t}(u_{\Delta t}(t), d_{\Delta t}(t)) \\ & - \frac{\Delta t}{2} H\tilde{H}^{-1}\mathcal{F}_{\Delta t}(t) + \frac{2}{\Delta t}\tilde{H}^{-1} g_{\Delta t}(t). \end{aligned}$$

Finally, we obtain

$$\begin{aligned} & g(\dot{u}_{\Delta t}(t+\Delta t), \dot{d}_{\Delta t}(t+\Delta t)) = \\ & \quad Qg(\dot{u}_{\Delta t}(t), \dot{d}_{\Delta t}(t)) + \frac{\Delta t}{2} Q\mathcal{F}_{\Delta t}(\dot{u}_{\Delta t}(t), \dot{d}_{\Delta t}(t)) \end{aligned} \tag{11}$$

where the matrix Q is defined by

$$Q = \left(I - H\tilde{H}^{-1}\right). \tag{12}$$

We proceed by recurrence to prove the required result. Expression (11) gives the result for $n = 1$ while the relation for $n = 0$ is trivial.

Let us suppose as true the relation for the order n. We have

$$\dot{g}_{\Delta t}(t + n\Delta t) = \frac{\Delta t}{2} \sum_{i=1}^{n} Q^i \mathcal{F}_{\Delta t}(t + \Delta t(n-i)) + Q^n \dot{g}_{\Delta t}(t).$$

We can compute the formula for $n + 1$:

$$G = \dot{g}_{\Delta t}(t + (n+1)\Delta t) = \dot{g}_{\Delta t}((t + n\Delta t) + \Delta t),$$

and by using (11) for $n = 1$, we obtain

$$\begin{aligned}
G &= Q\dot{g}_{\Delta t}(t+n\Delta t) + \frac{\Delta t}{2} Q\mathcal{F}_{\Delta t}(t+n\Delta t) \\
&= Q\left[\frac{\Delta t}{2}\sum_{i=1}^{n} Q^i \mathcal{F}_{\Delta t}(t+\Delta t(n-i)) + Q^n \dot{g}_{\Delta t}(t)\right] + \frac{\Delta t}{2} Q\mathcal{F}_{\Delta t}(t+n\Delta t) \\
&= \frac{\Delta t}{2}\sum_{i=1}^{n} Q^{i+1} \mathcal{F}_{\Delta t}(t+\Delta t(n-i)) + \frac{\Delta t}{2} Q\mathcal{F}_{\Delta t}(t+n\Delta t) + Q^{n+1}\dot{g}_{\Delta t}(t) \\
&= \frac{\Delta t}{2}\sum_{i=2}^{n+1} Q^{i} \mathcal{F}_{\Delta t}(t+\Delta t(n+1-i)) + \frac{\Delta t}{2} Q\mathcal{F}_{\Delta t}(t+n\Delta t) + Q^{n+1}\dot{g}_{\Delta t}(t)
\end{aligned}$$

Finally, we have

$$G = \frac{\Delta t}{2}\sum_{i=1}^{n+1} Q^{i} \mathcal{F}_{\Delta t}(t+\Delta t(n+1-i)) + Q^{n+1}\dot{g}_{\Delta t}(t).$$

■

So, if we assume that the constraint is verified at the initial state then for all $t = n\Delta t$ we have

$$\dot{g}_{\Delta t}(t) = \frac{\Delta t}{2}\sum_{i=1}^{n} Q^{i} \mathcal{F}_{\Delta t}(t-i\Delta t).$$

By putting this expression in equation (11), we obtain the following system

$$\left\{\begin{array}{ll}
m & \dfrac{\dot{d}_{\Delta t}(t+\Delta t) - \dot{d}_{\Delta t}(t)}{\Delta t} = \hat{f}_{\Delta t}(t) + \theta^{-1}\tilde{H}^{-1}\mathcal{F}_{\Delta t}(t) \\
 & +\dfrac{1}{2}\theta^{-1}\tilde{H}^{-1}\displaystyle\sum_{i=1}^{n} Q^i \mathcal{F}_{\Delta t}(t-i\Delta t) \\
M & \dfrac{\dot{u}_{\Delta t}(t+\Delta t) - \dot{u}_{\Delta t}(t)}{\Delta t} = \hat{F}_{\Delta t}(t) - \beta^{-1}A^t\tilde{H}^{-1}\mathcal{F}_{\Delta t}(t) \\
 & -\dfrac{1}{2}\beta^{-1}A^t\tilde{H}^{-1}\displaystyle\sum_{i=1}^{n} Q^i \mathcal{F}_{\Delta t}(t-i\Delta t).
\end{array}\right. \tag{13}$$

3.2 Governing equations

We have constructed the discrete equations verified by the solution in the coupling region. In particular, we have an explicit formula for the velocity update performed at each time step.

By classical analysis, the governing equations can be found from the velocity update by taking the limit as Δt goes to zero, which will provide the acceleration and hence the force. In our coupled study, the existence of the limit has to be proved and this is not trivial mainly because of the term $g(t)\Delta t^{-1}$. The purpose of this section is to proof the existence as well as to explicitly compute the value of this limit.

First, we introduce the following lemma:

Lemma 3.3 *Under the hypotheses:*

H1 $\begin{cases} u_{\Delta t}(t) \to u(t) \\ d_{\Delta t}(t) \to d(t) \end{cases}$ *when* Δt *tends towards* 0

H2 *The potentials used to compute the forces are* $\mathcal{C}^1(\mathbb{R}^+)$

then the function $\mathcal{F}_{\Delta t}(t)$ *converges to*

$$\tilde{\mathcal{F}}(u(t), d(t)) = AM^{-1}F(u(t)) - m^{-1}f(d(t))$$

when Δt *tends towards* 0.

The proof of this lemma is a simple use of the continuity of functions F and f and of the convergence of the trajectories.

We have to know the behavior of the constraints in order to verify that the integration scheme in the condensed case is coherent and converges. For this purpose we can use the following proposition:

Proposition 3.1 *Under the hypotheses*

H1 $\rho(I - H\tilde{H}^{-1}) < 1$

H2 *The potentials used to compute the forces are* $\mathcal{C}^1(\mathbb{R}^+)$ *and* F *and* f *are continuous functions*

H3 $\begin{cases} u_{\Delta t}(t) \to u(t) \\ d_{\Delta t}(t) \to d(t) \end{cases}$ *when* Δt *tends to* 0

H4 *The functions* $u(.)$ *and* $d(.)$ *are* $\mathcal{C}^1(\mathbb{R}^+)$

H5 *For all* Δt *we assume* $g(\dot{u}_{\Delta t}(0), \dot{d}_{\Delta t}(0)) = 0$

Then we have

$$\begin{aligned} \mathcal{H}(t) &= \lim_{\Delta t \to 0} \frac{g(\dot{u}_{\Delta t}(t), \dot{d}_{\Delta t}(t))}{\Delta t} \\ &= Q(I - Q)^{-1}\tilde{\mathcal{F}}(u(t), d(t)) \end{aligned}$$

where $Q = (I - H\tilde{H}^{-1})$.

Proof. According to (***H5***) and lemma (3.2), the constraint is satisfied at the initial state which gives for all given t with $t = n\Delta t$

$$\dot{g}_{\Delta t}(t) = \frac{\Delta t}{2} \sum_{i=1}^{n} Q^i \mathcal{F}_{\Delta t}(t - i\Delta t). \tag{14}$$

A first remark on this result is that the constraint depends on the evaluation of weighting differences between the continuum forces and the atomic forces that are evaluated in the computation of $\mathcal{F}_{\Delta t}$ at each time step. The second remark is that the sequence $(Q^i)_{i\in\mathbb{N}}$ is a geometrical one. Thus it converges only if $\| Q \| < 1$. Then, we conclude that the influence of a previous force gap at a given time step to the present time decreases like the geometrical sequence of multiplier Q.

We use now the fact that the function $\mathcal{F}(u(.), d(.))$ is continuously differentiable on the segment of time $[0, t]$ (***H4***) and by using lemma 3.3, one can deduce that there exists an upper bound Γ of the quantity $\| \mathcal{F}(u(t), d(t)) \|$. By using (***H4***), Γ can be chosen such that it bounds also to the quantities $\| \mathcal{F}_{\Delta t}(u_{\Delta t}(t), d_{\Delta} t(t)) \|$ on the interval $[0, t]$. Now let us consider the following sequence

$$u_n = \sum_{i=1}^{n} Q^i \mathcal{F}_{\Delta t}(t - i\Delta t) \qquad \forall n \in \mathbb{N}^\star.$$

Then, thanks to lemma 3.2 we have

$$u_n = \frac{2}{\Delta t}\, \dot{g}_{\Delta t}(n\Delta t) = \frac{2}{\Delta t}\, \dot{g}_{\Delta t}(t).$$

In other words, each iteration of the sequence is the value of twice the constraint function at time t divided by the time step t/n, considering that it is the result of n integration steps of size $\Delta t = t/n$.

We evaluate the difference

$$\mathcal{D}_n = u_n - \left[Q(I - Q)^{-1}\right] \tilde{\mathcal{F}}(u(t), d(t))$$

to show that it tends towards 0 when n tends towards ∞ and t fixed. We first transform this expression thanks to (***H1)*** by using the classical geometric series:

$$\sum_{i=1}^{\infty} Q^i = Q(I - Q)^{-1}.$$

Thus we have the following expression for $\mathcal{D}_n$

$$\mathcal{D}_n = \sum_{i=1}^{n} Q^i (\mathcal{F}_{\Delta t}(t - i\Delta t) - \tilde{\mathcal{F}}(u(t), d(t)) - \sum_{i=n+1}^{\infty} Q^i \tilde{\mathcal{F}}(u(t), d(t)).$$

We will decompose $\mathcal{D}_n$ in three terms and will find upper bounds for each one of them with respect to an arbitrary positive number ϵ. To obtain this decomposition, we will define the index m_ϵ by using the assumption (***H1***) such that:

$$\forall \epsilon > 0, \quad \exists m_\epsilon \in \mathbb{N} \quad / \quad \forall i \geq m_\epsilon \quad \| Q \|^i < \frac{\epsilon}{3\Gamma}(1 - \| Q \|). \tag{15}$$

We will see later why we made this particular choice as upper bound. From now, m_ϵ will remain fixed. Then, we have the following decomposition for all $m \geq m_\epsilon$

$$\mathcal{D}_n = \underbrace{\sum_{i=1}^{m} Q^i (\mathcal{F}_{\Delta t}(t - i\Delta t) - \tilde{\mathcal{F}}(u(t), d(t))}_{A_n} + \underbrace{\sum_{i=m+1}^{n} Q^i \mathcal{F}_{\Delta t}(t - i\Delta t)}_{B_n}$$
$$- \underbrace{\sum_{i=m+1}^{\infty} Q^i \tilde{\mathcal{F}}(u(t), d(t))}_{C_n}.$$

Our purpose is to bound the norm of $\mathcal{D}_n$ by ϵ. Thus convergence would be proved. Let us consider the first term A_n. We write:

$$\begin{aligned}
&\mathcal{F}_{\Delta t}(t-i\Delta t) - \tilde{\mathcal{F}}(u(t),d(t)) = \\
&\quad AM^{-1}\left[\frac{1}{2}F(u_{\Delta t}(t-i\Delta t)) + \frac{1}{2}F(u_{\Delta t}(t-(i-1)\Delta t)) - F(u(t))\right] \\
&\quad - m^{-1}\left[\frac{1}{2}f(d_{\Delta t}(t-i\Delta t)) + \frac{1}{2}f(d_{\Delta t}(t-(i-1)\Delta t)) - f(d(t))\right].
\end{aligned}$$

As the forces F and f are continuous (***H2***) and thanks to the convergence of the trajectories (***H3)***, one can apply lemma 3.3 to obtain

$$\mathcal{F}_{\Delta t}(t-i\Delta t) - \tilde{\mathcal{F}}(u(t),d(t)) \longrightarrow 0 \quad when \quad n \to \infty.$$

Thus it exists a function η which converges towards 0 when n tends towards infinity such that

$$\| A_n \| \leq \eta(n) \sum_{i=1}^{m} \| Q^i \| \leq \eta(n) \frac{(1- \| Q \|^{m+1})}{1- \| Q \|}.$$

We then have found an upper bound for A_n that is a function converging towards 0 when n tends to infinity. In other words,

$$\exists N \in \mathbb{N} \text{ such that } \forall n > N > m_\epsilon \ , \quad \| A_n \| \leq \frac{\epsilon}{3}.$$

Concerning the second term B_n, we use the following upper bound:

$$\| B_n \| \leq \sum_{i=m+1}^{n} \| Q \|^i \| \mathcal{F}_{\Delta t}(t-i\Delta t) \| \leq \Gamma \sum_{i=m+1}^{\infty} \| Q \|^i \leq \Gamma \frac{\| Q \|^{m+1}}{1- \| Q \|}.$$

Moreover the choice of m_ϵ, the relation (15) and the above upper bound imply

$$\| B_n \| \leq \frac{\epsilon}{3}.$$

Finally, we treat in a similar way the last term C_n. We have

$$\| C_n \| \leq \sum_{i=m+1}^{\infty} \| Q^i \| \| \tilde{\mathcal{F}}(u(t),d(t)) \| \leq \Gamma \frac{\| Q \|^{m+1}}{1- \| Q \|} \leq \frac{\epsilon}{3}.$$

Finally, we obtain

$$\forall \epsilon > 0 \ , \quad \exists m_\epsilon \ , \quad \text{such that } \forall n > m_\epsilon \text{ we have } \| D_n \| \leq \epsilon.$$

That ends the proof of proposition 3.1. ■

We found that the continuous expression of the additional force added in the governing equations is

$$\mathcal{H}(t) = Q(I-Q)^{-1}\tilde{\mathcal{F}}(u(t),d(t)) = \left[\tilde{H}H^{-1} - I\right]\tilde{\mathcal{F}}(u(t),d(t)).$$

As we can see, if we don't use the lumped constraint approximation there is no additional force in the system.

With the assumption of linearized forces and considering K^C the stiffness matrix for continuum mechanics and K^A the stiffness matrix for molecular dynamics, the expression of $\tilde{\mathcal{F}}(u(t), d(t))$ becomes

$$\tilde{\mathcal{F}}(u(t), d(t)) = AM^{-1}K^C u(t) - m^{-1}K^A d(t).$$

Then $\mathcal{H}(t)$ can be rewritten as

$$\mathcal{H}(t) = (\tilde{H}H^{-1} - I)\left[AM^{-1}K^C u(t) - m^{-1}K^A d(t)\right].$$

Now, we introduce these additional forces into the equations of the constrained velocity update (13) and we obtain the limit behavior when Δt tends toward zero

$$\left\{\begin{array}{l} m\,\ddot{d}(t) = (I - \theta^{-1}H^{-1}m^{-1})K^A d(t) + \theta^{-1}H^{-1}AM^{-1}K^C u(t) \\ \quad +\theta^{-1}H^{-1}(\tilde{H}H^{-1} - I)\left[AM^{-1}K^C u(t) - m^{-1}K^A d(t)\right] \\ M\,\ddot{u}(t) = (I - \beta^{-1}A^t H^{-1}AM^{-1})K^C u(t) + \beta^{-1}A^t H^{-1}m^{-1}K^A d(t) \\ \quad -\beta^{-1}A^t H^{-1}(\tilde{H}H^{-1} - I)\left[AM^{-1}K^C u(t) - m^{-1}K^A d(t)\right]. \end{array}\right.$$

After reduction we have

$$\left\{\begin{array}{ll} m\,\ddot{d}(t) & = (I - \theta^{-1}H^{-1}\tilde{H}H^{-1}m^{-1})K^A d(t) + \theta^{-1}H^{-1}\tilde{H}H^{-1}AM^{-1}K^C u(t) \\ M\,\ddot{u}(t) & = (I - \beta^{-1}A^t H^{-1}\tilde{H}H^{-1}AM^{-1})K^C u(t) + \\ & \qquad\qquad \beta^{-1}A^t H^{-1}\tilde{H}H^{-1}m^{-1}K^A d(t) \end{array}\right. \tag{16}$$

Remark: *when $\tilde{H}$ is equal to H then the term $(\tilde{H}H^{-1} - I)$ vanishes, and this shows the consistency of the expression (16).*

Let us now introduce the notations

$$\begin{array}{ll} C_{11} & = (I - \theta^{-1}H^{-1}\tilde{H}H^{-1}m^{-1})K^A, \quad C_{12} = \theta^{-1}H^{-1}\tilde{H}H^{-1}AM^{-1}K^C, \\ C_{21} & = \beta^{-1}A^t H^{-1}\tilde{H}H^{-1}m^{-1}K^A, \quad C_{22} = (I - \beta^{-1}A^t H^{-1}\tilde{H}H^{-1}AM^{-1})K^C, \end{array}$$

to obtain the system

$$\begin{pmatrix} m & 0 \\ 0 & M \end{pmatrix}\begin{pmatrix} \ddot{d} \\ \ddot{u} \end{pmatrix} = \begin{pmatrix} C_{11} & C_{12} \\ C_{21} & C_{22} \end{pmatrix}\begin{pmatrix} d \\ u \end{pmatrix}. \tag{17}$$

This is a typical PDE easily linked to an oscillator system. Thus we can study the modes of such an oscillator.

We have shown that a force is added to the DOFs of the system proportionally to the value of the constraint. When we condense the constraint matrix the constraints are not exactly satisfied, and we thus introduce an error which behaves as a diffusion force. On the other hand, the expression of the constraint depends on all the time steps of the simulation, called hereafter the history of the simulation. We have found a behavior at the limit when the time step tends towards 0. Nowadays, we cannot use a too small time step in our numerical simulations. The matrix Q will quantify if our analysis will be valid or not. However, in order to analyze the modes, it is necessary to consider the behavior at the limit. In practice, if the norm of Q is too close to 1, then the terms of the series (14) converge slowly, giving an huge importance to the history, while the limit behavior neglects it.

To conclude this section, our theoretical approach brings a very fine comprehension of the phenomena involved in the coupling. However, we use a continuous behavior in time for our system. In the following, we will exploit this

theoretical analysis on various cases. We will then highlight the configurations of the coupling which are source of wave reflections. We will also study how the condensation of the constraint matrix plays an important part in the quality of such a coupling method.

4 Spectral results

Before discussing the numerical results, we present first the process that was used to analyze the spectral characteristics of our coupling method.

As the governing equations for the coupling system are given by (17), we will naturally be interested by the eigenvalues of the following matrix S

$$S = \begin{pmatrix} m & 0 \\ 0 & M \end{pmatrix}^{-1} \begin{pmatrix} C_{11} & C_{12} \\ C_{21} & C_{22} \end{pmatrix}.$$

We will then determine the modes admitted by the coupled material with eigenvalue computations. As the eigenvalues can be complex, we separate the interpretation of the real and imaginary part of the modes. Indeed, the eigenvalues are written in polar coordinates such as $\omega_k^2 = \rho e^{i\theta}$. The modes generate normalized solutions of the form $V_\omega e^{i\omega t}$ and we distinguish atomic part V_ω^A from finite element part V_ω^C for each eigenvector. Then, the only valid modes are the ones for which the imaginary part is negative: we have $\omega = \sqrt{\rho} e^{\theta/2+c\pi} = a + ib$ where c is selected such that $b < 0$. By separating the atomic part from the finite element part of the eigenvectors, the normalized solutions is

$$\begin{pmatrix} V_\omega^A \\ V_\omega^C \end{pmatrix} e^{-iat} e^{bt}$$

and the imaginary part b refers to the dissipative factor of a given complex mode.

In the following, we consider the case of a coupling zone of size 104 r_0 including 104 atoms, and a finite element zone containing 13 finite elements and 14 nodes each of them with a size $h = 8r_0$. Then the matrix S is squared and of size $104 + 14 = 118$.

4.1 Spectrum modes of the coupling model

We compute the spectrum associated to the coupling model and we compare it with the ones associated with the full finite element model and the full atomic chain. The results are presented in figure 13. In the case of the studied mesh, the cutoff frequency for the finite element model is $2.75\,10^{12}$. It is straightforward that the cutoff frequency, and more generally the spectrum, is related to the finite element size. We discuss this point in section 4.4. The cutoff frequency of the atomic model is $2.23\,10^{13}$ and it is naturally related to the Brillouin zone, then having a wavelength of r_0. These two frequencies are important as they limit the vibrations of both models when they are not coupled. The band of frequencies between these two values delimit the frequencies that should be absorbed because the full finite element model cannot propagate such high frequency waves. Indeed, this is mostly because the mesh used does not have a sufficient number of nodes to represent those waves, as it can be seen from the dispersion equations of both models (see [3]).

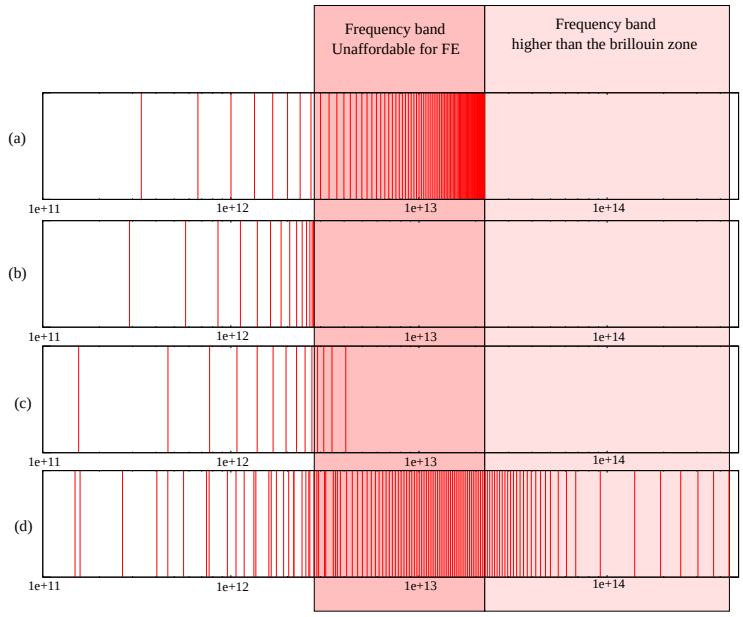

Figure 13: Spectrum of a monoatomic chain constituted of 104 atoms (a), of a 1D homogeneous grid with finite element size of $h = 8r_0$ (b), and of the coupling model in its complete (c) and its condensed form (d).

Now, if we consider the spectrum of the coupling method when the constraint matrix is not condensed, it can be observed that the cutoff frequency has been slightly moved forward to the value $4.08\,10^{12}$. The consequence of such a modification is that mesh nodes are allowed to vibrate at higher frequencies than when they are not coupled. But in the same way, this cutoff frequency is also respected for the atomic DOFs, preventing atoms to vibrate at high frequencies. In other words, waves coming to the coupling zone at frequencies higher than $4.08\ 10^{12}$ will not be allowed to propagate into the coupling zone, inducing a wave reflection by wave scattering ([16]).

In comparison, the condensation of the constraint matrix strongly modifies the spectrum of the coupling by moving up to $4.45\ 10^{14}$ radian per seconds. Clearly, this gives a justification concerning the positive effect of the constraint condensation for the wave reflection problem as both atoms and finite elements are theoretically allowed to vibrate until the Brillouin zone.

The theoretically admitted frequencies above the Brillouin zone are not valid. In that manner, it seems interesting to consider the dissipation coefficient of each mode, the dissipation power, and the properties of the associated eigenvectors, and finally the transmission power. This is the subject of the two following sections.

4.2 Dissipation of the coupling model

In this section, we first present the modes plotted as impulses where the height of each impulse will be associated to the mode imaginary part. Figures 14 and

15 present the modes computed without condensation and with condensation respectively.

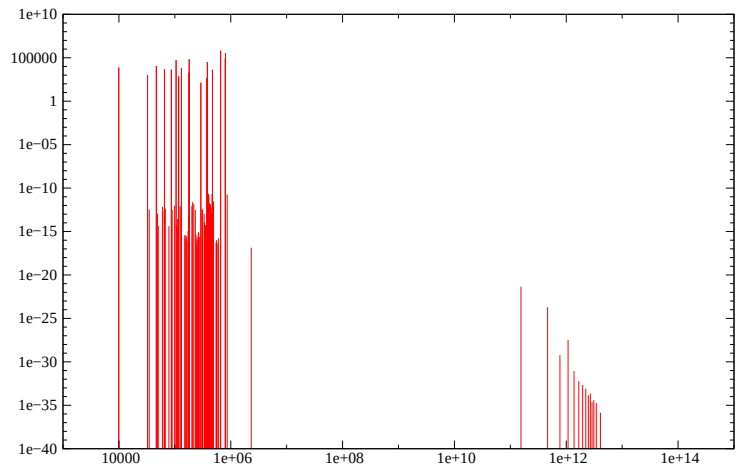

Figure 14: Dissipation power of the admitted modes for the non-condensed coupling model.

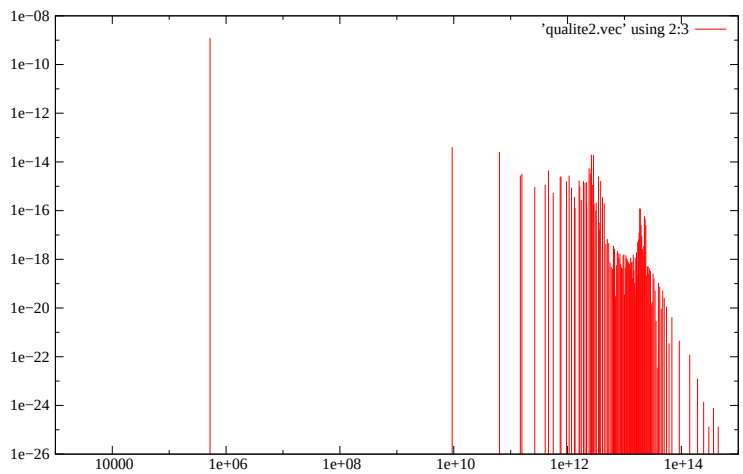

Figure 15: Dissipation power of the admitted modes for the condensed coupling model.

Concerning both figures, our first remark is that the dissipation power is very low. In the non-condensed case, the maximal dissipation power is about 6.42 10^5 for an associated frequency of 6.59 10^5. Indeed, if we consider magnitude decreasing ratio r after a time t, we have

$$r = e^{-bt} \longrightarrow t = -ln(r)/b.$$

Then for a decreasing ratio of 90%, a time of the order of $t = -ln(0.1)/10^5 = 2.302\ 10^{-5}$ is necessary. As we have to consider usual molecular dynamics time step of the order of the femtosecond, the necessary time is unreachable.

Furthermore, the frequency of the mode of highest dissipation ratio is a very low one. Moreover the wavelengths associated with these low frequencies are much more higher than the size of the studied coupling zone. This totally excludes that this mode can be responsible for the energy dissipation observed in our simulations. In the condensed case, the maximal dissipation power is $1.22\ 10^{-9}$ for an associated frequency of $5.22\ 10^{5}$ which is a lower dissipation power. Then it can be concluded that the absorption observed in simulations cannot be explained by dissipation effects.

4.3 Transmission of the coupling model

Beside the dissipative effects, the transmission from one model to the other for each mode must be considered. Indeed, since the shape of the eigenvectors influences the wave transmission through the coupling, it is interesting to compare the respective norms of each of these parts. We define the transmission power by

$$T(\omega) = \frac{\| V_\omega^C \|}{\| V_\omega^A \|}. \tag{18}$$

This measurement is justified by the fact that we wish to evaluate how the atomic vibrations are transmitted into mesh node vibrations. Figure 16 presents the transmission power of the modes in the range $[1\,10^{11}, 2.23\,10^{12}]$ for both condensed and not-condensed cases. The first observation concerns the not-condensed modes for which the transmission power is increasing until the cutoff frequency mode. This means that the transmission is maximal around that cutoff area. On the contrary, in the condensed case, the transmission power is decreasing until the previously mentioned frequency. This clearly shows a different behavior of our oscillator system in the problematic frequency band.

4.4 Correlation with finite element size

The results achieved from the simulation presented by figure 10 show that some wave reflections still occur around a wave length of $14r_0$ which corresponds to a frequency of $3.47\ 10^{12}$ radian per seconds according to atomic chain dispersion law [3]. Neither dissipation power nor transmission power can clearly explain this localized reflection rate. The spectrum study, presented in the previous sections, must take into account that the system we are studying is a stimulated oscillator. Then, the behavior of such a system is not the one of a freely evolving one. This prevents us to have clear explanations of the reflection magnitudes or even the knowledge of the stimulated modes with respect to a given stimulation frequency.

But there is one additional parameter that strongly influences the reflection rates, that is the finite element size. To point out this, we performed measurements with different finite element sizes. The results are presented by figure 17 for a condensed constraint matrix. Clearly we can see the dependence on finite element size despite the fact that the spectrum is extended by the condensation of the constraint matrix.

Without any clue from the spectral study, we can still bring some information about the frequency where the peaks of wave reflections are observed. We can see that the cutoff frequency of the finite element model, the cutoff frequency of the coupled model without lumped matrix and the frequency at which

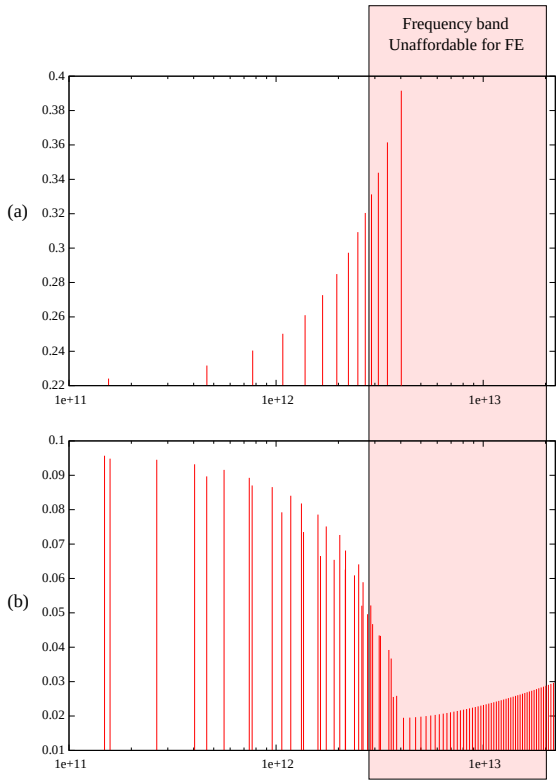

Figure 16: (a) Transmission power of each mode for a coupling model with a full constraint matrix. (b) Transmission power of each mode with a condensed constraint matrix.

reflection peaks are observed (with lumped matrix) are in a constant interval. Table 18 presents these relevant frequencies for various finite element sizes. The frequencies associated to the reflection peaks where computed by inversion of the dispersion equation for atomic chain. These numbers give us an intuitive solution to understand what is occurring in such coupled simulations: the finite element model is entering into resonance for a precise stimulation frequency. To prove that, our spectral interpretation of the oscillator should be extended with a dissipation/friction function in order to avoid energy accumulation in the coupled zone. Indeed, without an energy dissipation any mode have an infinite resonance.

4.5 Study of the dependence on the past history

The constraint matrix condensation changes radically the rates of wave reflections. As we showed in section 3, condensation induces one additional force which is proportional to the value of the constraint applied on the velocities. This force acts like a diffusion force always within the limit of the linear approximation of the forces.

It is pointed out that under the condensation assumption, the governing equation is given by (16). Concretely, in the case of discrete time integration,

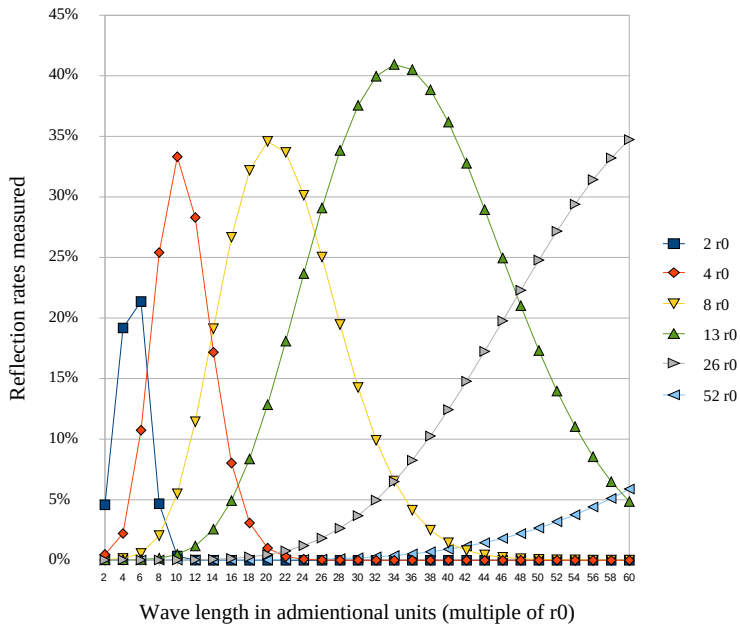

Figure 17: Reflection rates measured with respect to injected wavelength for a bridging zone of size $104r_0$. We present the reflection rates for six finite element sizes: $2r_0$, $4r_0$, $8r_0$, $13r_0$, $26r_0$ and $52r_0$.

FE size	Cutoff FE	Cutoff coupling	reflection peak
$2r_0$	$1.11\ 10^{13}$	$1.47\ 10^{13}$	$1.30\ 10^{13}$ ($\lambda = 5r_0$)
$4r_0$	$5.52\ 10^{12}$	$8.14\ 10^{12}$	$6.86\ 10^{12}$ ($\lambda = 10r_0$)
$8r_0$	$2.75\ 10^{12}$	$4.08\ 10^{12}$	$3.47\ 10^{12}$ ($\lambda = 20r_0$)
$13r_0$	$1.68\ 10^{12}$	$2.46\ 10^{12}$	$2.04\ 10^{12}$ ($\lambda = 34r_0$)
$26r_0$	$8.22\ 10^{11}$	$1.17\ 10^{12}$	$1.12\ 10^{12}$ ($\lambda = 62r_0$)
$52r_0$	$3.93\ 10^{11}$	$5.52\ 10^{11}$	—

Figure 18: Cutoff frequencies for finite element model, coupled model and in the last column frequencies with highest reflection rates.

the value of the constraint at time $t = n\Delta t$ is

$$\dot{g}(t) = \frac{\Delta t}{2} \sum_{i=1}^{n} Q^i \mathcal{F}_{\Delta t}(t - i\Delta t)$$

which can be assumed to be a temporal convolution. Then, we are interested in the matrix Q defined by (12), and particularly by its eigenvalues which grant convergence of *history*. The *history* notion is related to the influence of constraint values of all steps preceding the current simulation time.

In section 3, we discussed the influence of the weighting of DOFs on the boundary condition. The cases studied until now were such that no atom is positioned exactly on the border of the bridging zone, thus avoiding a null weighting. On the other hand, for the first node of the mesh, one must choose a weighting value which is not zero. So far, we have considered a coefficient

of 10^{-3} as suggested by the authors of [7]. But we observed that the weight associated with the first node of the coupling modifies the eigenvalues of Q and has a strong influence on the treatment of wave reflections. From now, we will name this weight value as "history factor". The choice of this denomination will be justified later. In the following, we will study the relation between the eigenvalues of the Q matrix and the history factor before providing reflection rates induced by a variation of this factor.

4.5.1 Eigenvalues of the matrix Q

We consider the atomic chain containing 104 atoms into the bridging zone which is coupled with a uniform finite element grid with $h = 8r_0$. To give comparative data, the weight of the second finite element node takes the value $h/R = 8r_0/104r_0 = 0.076$. With an history factor of 10^{-3}, the eigenvalues of the matrix Q are contained in the interval $[4.33\ 10^{-16}, 9.98\ 10^{-1}]$. This information is important, because according to lemma 3.2, the influence of a contribution at time step i to the history is weighted by Q^{j-i} where j is the current time step. Then we have for a given upper bound 10^{-a} of the eigenvalues:

$$\lambda_{max}^{j-i} \leq 10^{-a}$$
$$j - i \leq -a\frac{ln(10)}{ln(\lambda_{max})}$$

where λ_{max} is the maximal eigenvalue of the matrix Q. Then, reaching an attenuation factor of 10^{-5} for a contribution to the history requires 6031 time steps to obtain it. This quantity will be referred as the *size of the history*. Another way to understand the importance of this quantity would be to consider it as the size of a sliding window that encompasses the past computations that influence the present situation.

The important point here is that the history factor modifies the eigenvalues and obviously the size of the history. Table 19 presents the history factor, the related maximal eigenvalue of matrix Q and the history size. We observe a decreasing behavior of the history size with respect to the history factor.

4.5.2 Reflection rates with respect to the history factor

The history factor, beside modifying the history size, is influencing the reflection rates. The effect of the history factor on wave reflection rates is presented on figure 20. The reflection rates are measured for the following history factors: $2\ 10^{-4}$, $6\ 10^{-4}$, $1\ 10^{-3}$, $6\ 10^{-3}$, 10^{-2} and $2\ 10^{-2}$. We have then different reflection rates according to these history factors. Mainly, the best solution with respect to magnitude of the reflections is given by an history factor value of $2\ 10^{-2}$, yielding a maximum at 28%. But this solution induces more reflections in the high frequencies. A factor of 10^{-3} gives good results with a maximum of 35% reflection rate and no reflections in the high frequency bandwidth. As a compromise between magnitude and high frequency treatment, the factor $6\ 10^{-3}$ has a maximal rate at 30% while the reflection increase in the high frequencies overcomes the solution of 10^{-3} by only a few percents. This clearly demonstrates again that the choice of this parameter should not be chosen arbitrarily.

history factor	maximal eigenvalue	size of history
10^{-10}	0.9999999998	$6.02\ 10^{10}$
10^{-9}	0.999999998	$6.02\ 10^{9}$
10^{-8}	0.99999998	$6.02\ 10^{8}$
10^{-7}	0.9999998	$6.02\ 10^{7}$
10^{-6}	0.999998	$6.02\ 10^{6}$
10^{-5}	0.99998	$6.02\ 10^{5}$
10^{-4}	0.9998	$6.02\ 10^{4}$
10^{-3}	0.998	$6.03\ 10^{3}$
10^{-2}	0.98	$6.17\ 10^{2}$
10^{-1}	0.92	$1.41\ 10^{2}$

Figure 19: Maximal and minimal eigenvalues of the matrix Q with respect to the weighting of the first node of the bridging zone. The size of the history is also presented as the number of time steps necessary to obtain a decreasing factor 10^{-5}.

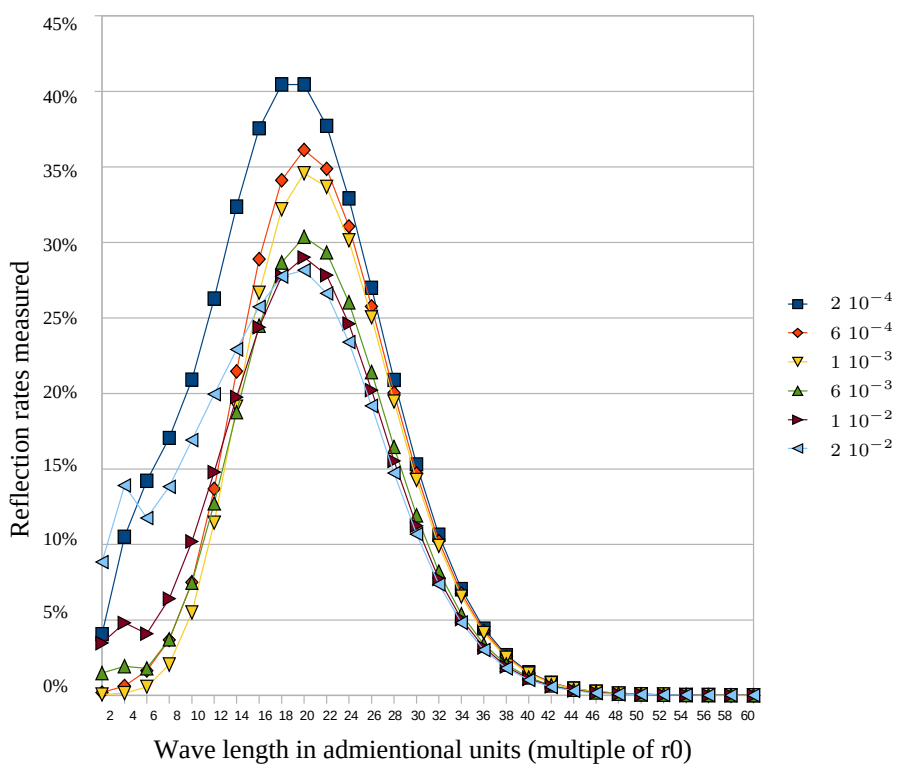

Figure 20: Reflection rates measured with respect to weight associated with first node in the bridging zone.

We tried to explain such a behavior by the spectral approach used until now. On figure 21, we report the transmission power of the modes obtained

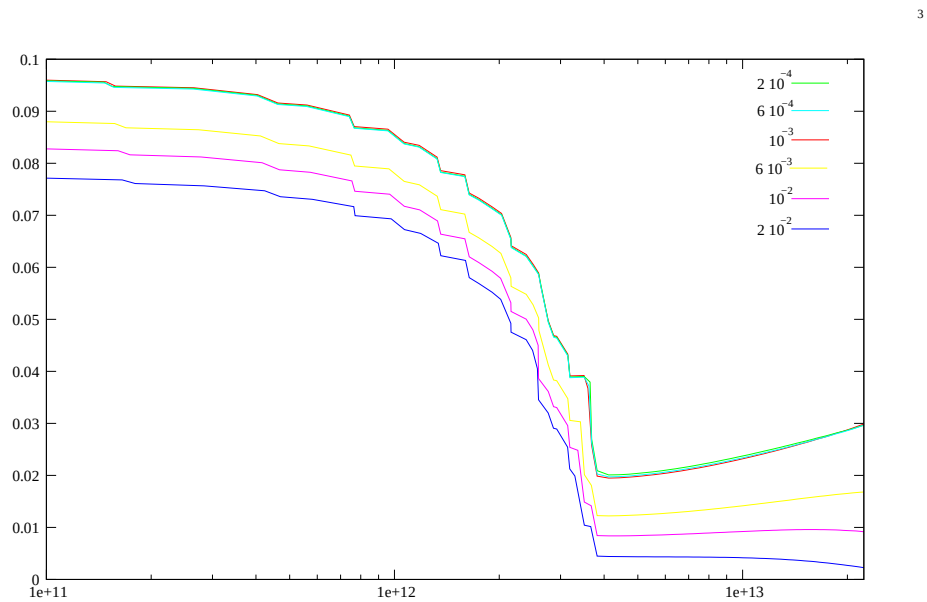

Figure 21: Spectral transmission power with respect to the history factors. Injected history factors are 2 10^{-4}, 6 10^{-4}, 1 10^{-3}, 6 10^{-3}, 1 10^{-2} and 2 10^{-2}.

with various history factors. We clearly see the influence of this parameter: the lower the factor is, the lower the transmission power will be. Still, the curves associated with the factors 2 10^{-4}, 6 10^{-4} and 1 10^{-3} are really close in comparison to the measured reflection rates.

In our model, the lack of understanding of this effect is due to the fact that the governing equation used to compute the spectrum is valid in the limit where the time step is going to zero. This limit behavior assumes that we neglect the difference of the history sizes as a zero time step implies an infinite number of iterations for the contraint value

$$\dot{g}(t) = \frac{\Delta t}{2} \sum_{i=1}^{n} Q^i \mathcal{F}_{\Delta t}(t - i\Delta t)$$

also providing zero contraint values. But all the simulations for the measurement of the reflection rates used an identical finite time step. It could be interesting, but really computational intensive, to measure the reflection rates with time steps adapted to the history sizes.

5 Conclusion

We have given a detailed description of the phenomena induced by the Bridging Method. We proposed an approximation of the coupling scheme with a controlled impact on the wave reflections, also measured on numerical 1D simulations. We verified that the condensation of the constraint matrix leads to forces with a variable importance related to the past of the trajectories, according to the so-called *history factor*. We observed the modifications of the

spectrum and transmission power due to that parameter, but these results do not allow - in the current state - to explain exactly all the observed modifications of the reflection rate curves. Moreover, our theoretical approach does not permit to understand the magnitude of the differences that are measured.

Despite these points, we observed clearly that the problematic zone is directly related to the finite element size since it fixes the cutting frequency for the finite element model, and we linked that frequency to the reflection peaks thanks to simulation benchmarks. Then, this study brings helpful information to adapt the size of the finite elements according to the problem which is studied in the atomistic zone and to the wave frequencies that will be generated.

Because of the nature of the true problem - the wave reflections - it would be interesting to consider an integration scheme with two distinct integration time steps, one for molecular dynamics and one for continuum mechanics. Indeed, it is intuitive that the treatment of the waves at the coupling interface will (pseudo)average the atomic trajectories to transfer to acceptable mesh node vibrations. The history size, the finite element size, and all the various parameters studied here are responsible for the transfer quality ; results of some really complex effects as demonstrated by our study. The authors of the method already suggested to use such a multi-time step algorithm, but with no other justification than the computational gain. The spectral consideration of such a scheme is expected to improve the reflections at some point, but the right choice of both time step, will need some investigation.

Finally, we have to say that the *Bridging Method* is generic enough to deal with any material, without any periodic assumption, which is a sufficient motivation in trying to improve it. Still, the original formulation uses a weighting of the Hamiltonians and will finally constrain only the velocities. We used an approximation where the governing equation is most likely a Newton one, with spatially weighted constraint corrections. It seems to be better if such a constraint is not completely respected (condensation of the constraint matrix), as we have proved in order to obtain lower reflection rates. This shows that the transfer between the scales have to consider an *history window*. Obviously the mesh nodes should not be constrained to instantaneous and high frequency atomic trajectories. Then the future of this method might be to consider that coupled models are constrained through kinetic energy. This could allow us to filter mechanical waves and eventually split the energy of incoming waves into thermal and strain energy contributions, according to the finite element sizes at the interface. This is an interesting direction to finite temperature multiscale simulations.

Acknowledgments The authors wish to acknowledge Adam Larat for useful discussions on the oscillator model developed here. We also acknowledge Christophe Denoual for many useful discussions on molecular dynamics and finite elements topics.

References

[1] F. F. Abraham, *How fast can cracks move? A research adventure in*

materials failure using millions of atoms and big computers, Advances in Physics, 52 (2003), pp. 727–790.

[2] M. P. Allen and D. J. Tildesley, *Computer Simulation of Liquids*, Oxford University Press, 1989.

[3] G. Anciaux, *Simulation multi-échelles des solides par une approche couplée dynamique moléculaire / éléments finis. De la modélisation à la simulation haute performances*, PhD thesis, Université Bordeaux 1, July 2007.

[4] S. Badia, M. Parks, P. Bochev, M. Gunzburger, and R. Lehoucq, *On atomistic-to-continuum coupling by blending*, Multiscale Modeling and Simulation, 7 (2008), pp. 381–406.

[5] P. T. Bauman, H. Ben Dhia, N. Elkhodja, J. Tinsley Oden, and S. Prudhome, *On the application of the arlequin method to the coupling of particle and continuum models*, Computational mechanics, 42 (2008).

[6] T. Belytschko, W. K. Liu, and B. Moran, *Finite Elements for Nonlinear Continua and Structures*, John Wiley & Sons, 2001.

[7] T. Belytschko and S. P. Xiao, *Coupling methods for continuum model with molecular model*, International Journal for Multiscale Computational Engineering, 1 (2003), pp. 115–126.

[8] J. Q. Broughton, F. F. Abraham, N. Bernstein, and E. Kaxiras, *Concurrent coupling of length scales: Methodology and application*, Physical Review B, 60 (1999), pp. 2391–2403.

[9] S. Curtarolo and G. Cede, *Dynamics of an inhomogeneously coarse grained multiscale system*, Physical Review Letters, 88 (2002).

[10] W. A. Curtin and R. E. Miller, *Atomistic/continuum coupling in computational materials science*, Modelling and simulation in materials science and engineering, 11 (2003), pp. R33–R68.

[11] S. Elliot, *The physics and chemistry of solids*, John Wiley & Sons, 1998.

[12] C. Kittel, *Introduction to Solid State Physics*, Wiley international edition, 2005.

[13] B. Q. Luan, S. Hyun, J. F. Molinari, M. O. Robbins, and N. Bernstein, *Multiscale modeling of two-dimensional contacts*, Physical Review E, 74 (2006).

[14] R. E. Miller and E. B. Tadmor, *The quasicontinuum method: Overview, applications and current directions*, Journal of Computer-Aided Materials Design, 9 (2003), pp. 203–239.

[15] S. Qu, V. Shastry, W. A. Curtin, and R. E. Miller, *A finite-temperature dynamic coupled atomistic/discrete dislocation method*, Modelling Simul. Mater. Sci. Eng., 13 (2005), pp. 1101–1118.

[16] R. E. Rudd and J. Q. Broughton, *Coarse-grained molecular dynamics and the atomic limit of finite elements*, Physical Review B, 58 (1998).

[17] J. Ryckaert, G. Ciccotti, and H. J. C. Berendsen, *Numerical integration of the cartesian equations of motion of a system with constraints: molecular dynamics of n-alkanes*, J. Comp. Phys., 23 (1977), pp. 327–341.

[18] E. B. Tadmor, M. Ortiz, and R. Phillips, *Quasicontinuum analysis of defects in solids*, Philosophical Magazine, 73 (1996), pp. 1529–1563.

[19] C. Yang, U. Tartaglino, and B. N. J. Persson, *A multiscale molecular dynamics approach to contact mechanics*, The European Physical Journal E - Soft Matter, 19 (2006), pp. 47–58.

Centre de recherche INRIA Bordeaux – Sud Ouest
Domaine Universitaire - 351, cours de la Libération - 33405 Talence Cedex (France)

Centre de recherche INRIA Grenoble – Rhône-Alpes : 655, avenue de l'Europe - 38334 Montbonnot Saint-Ismier
Centre de recherche INRIA Lille – Nord Europe : Parc Scientifique de la Haute Borne - 40, avenue Halley - 59650 Villeneuve d'Ascq
Centre de recherche INRIA Nancy – Grand Est : LORIA, Technopôle de Nancy-Brabois - Campus scientifique
615, rue du Jardin Botanique - BP 101 - 54602 Villers-lès-Nancy Cedex
Centre de recherche INRIA Paris – Rocquencourt : Domaine de Voluceau - Rocquencourt - BP 105 - 78153 Le Chesnay Cedex
Centre de recherche INRIA Rennes – Bretagne Atlantique : IRISA, Campus universitaire de Beaulieu - 35042 Rennes Cedex
Centre de recherche INRIA Saclay – Île-de-France : Parc Orsay Université - ZAC des Vignes : 4, rue Jacques Monod - 91893 Orsay Cedex
Centre de recherche INRIA Sophia Antipolis – Méditerranée : 2004, route des Lucioles - BP 93 - 06902 Sophia Antipolis Cedex

Éditeur
INRIA - Domaine de Voluceau - Rocquencourt, BP 105 - 78153 Le Chesnay Cedex (France)
http://www.inria.fr
ISSN 0249-6399